Computer Methods in Biomechanics and Biomedical Engineering

Verification and comparison of four numerical schemes for a 1D viscoelastic blood flow model

Xiaofei Wang[a], Jose-Maria Fullana[a] & Pierre-Yves Lagrée[b]

[a] Sorbonne Universités, UPMC Univ Paris 6, UMR 7190, Institut Jean le Rond d'Alembert, Paris, France

[b] CNRS, UMR 7190, Institut Jean le Rond d'Alembert, Paris, France
Published online: 22 Aug 2014.

PLEASE SCROLL DOWN FOR ARTICLE

Taylor & Francis
Taylor & Francis Group

Verification and comparison of four numerical schemes for a 1D viscoelastic blood flow model

Xiaofei Wang[a]*, Jose-Maria Fullana[a1] and Pierre-Yves Lagrée[b2]

[a]Sorbonne Universités, UPMC Univ Paris 6, UMR 7190, Institut Jean le Rond d'Alembert, Paris, France;
[b]CNRS, UMR 7190, Institut Jean le Rond d'Alembert, Paris, France

A reliable and fast numerical scheme is crucial for the 1D simulation of blood flow in compliant vessels. In this paper, a 1D blood flow model is incorporated with a Kelvin–Voigt viscoelastic arterial wall. This leads to a nonlinear hyperbolic–parabolic system, which is then solved with four numerical schemes, namely: MacCormack, Taylor–Galerkin, monotonic upwind scheme for conservation law and local discontinuous Galerkin. The numerical schemes are tested on a single vessel, a simple bifurcation and a network with 55 arteries. The numerical solutions are checked favorably against analytical, semi-analytical solutions or clinical observations. Among the numerical schemes, comparisons are made in four important aspects: accuracy, ability to capture shock-like phenomena, computational speed and implementation complexity. The suitable conditions for the application of each scheme are discussed.

Keywords: blood flow; 1D flow modeling; vascular network; numerical simulation

1. Introduction

Simulating the blood flow in compliant vessels is of great clinical relevance and is also a challenging problem. Many 3D simulations of this fluid–structure interaction (FSI) are presented in the literature (Perktold and Rappitsch 1995; Di Martino et al. 2001; Gerbeau et al. 2005; Li and Kleinstreuer 2005; Torii et al. 2006; Crosetto et al. 2011; Bertoglio et al. 2012). Nevertheless they are known to be time and memory consuming and therefore most of them are restricted to local positions (i.e. single vessel and confluences) or a few vessel segments. Although modeling techniques and computational efficiency are constantly improved, a 3D simulation of the FSI in a large network of compliant vessels is still prohibitive. Reduced models have been derived by taking advantage of the physics of the blood flow in large vessels. If we assume an axisymmetric circular velocity profile in the vessel, the 3D problem can be reduced to a 2D problem. If we further assume that the wavelength is large compared to the radius of the vessel, a 1D model can be obtained. The 1D model is specially interesting for several reasons. First, this model captures well the behaviors of pulse wave, from which one can extract a lot of useful information about the cardiovascular system. For example, the pulse wave velocity has been recognized by European Society of Hypertension as a very important marker to the diagnosis and treatment of hypertension (Blacher et al. 1999; Mancia et al. 2007). Second, it allows fast numerical computation, which permits real-time applications for medical planning. Third, it also provides pertinent boundary conditions

(BCs) for 3D simulations in multi-scale models (Formaggia et al. 2001; Nobile 2009).

The 1D model consists of a system of two partial differential equations (PDEs) for the conservation of mass and momentum. The PDEs involve the flow rate Q, the cross-sectional area A and the average pressure P. To close the system, the constitutive relation of the arterial wall which relates P and A is necessary. After the insertion of this relation into the PDEs, a nonlinear hyperbolicity-dominated system is obtained. Depending on the details of the modeling, there may be some additional terms. Diffusive terms can appear due to an additional fluid viscous term (Hughes and Lubliner 1973; Vignon and Taylor 2004) or/and the wall viscoelasticity (Formaggia et al. 2003). The axial pre-stress of the wall or/and the wall inertia can lead to dispersive operators (Formaggia et al. 2003).

In case of weak nonlinearity (i.e. small perturbation around the equilibrium state (Pedley 1980; Lighthill 2001)), we can linearize the 1D governing equations and find analytical solutions in the frequency domain (Wang and Parker 2004; Nicoud et al. 2005). But for the full nonlinear system, analytical solutions are not available yet. Thus several numerical schemes have been proposed and used to solve the system in time domain. We roughly classify them as follows:

- Finite difference (FD) (Zagzoule and Marc-Vergnes 1986; Elad et al. 1991; Stergiopulos et al. 1992; Olufsen et al. 2000; Pullan et al. 2002; Reymond et al. 2009; Saito et al. 2011).
- Finite volume (FV) (Wibmer 2004; Cavallini et al. 2008; Delestre and Lagrée 2012).

- Finite element (FE) (Formaggia et al. 2003; Sherwin et al. 2003; Vignon and Taylor 2004; Alastruey et al. 2011; Malossi et al. 2012)
- Discontinuous Galerkin (DG) (Sherwin et al. 2003; Matthys et al. 2007; Mynard and Nithiarasu 2008; Marchandise et al. 2009; Alastruey et al. 2011)

These schemes have been successfully applied in other communities where researchers have to solve similar hyperbolic problems. For instance, the MacCormack scheme (FD) was principally designed for gas dynamics (i.e. 1D compressible Euler equations) and it was then successfully used to compute blood flow (Elad et al. 1991; Fullana and Zaleski 2009). From ideas frequently applied in shallow water equations, Delestre and Lagrée (2012) obtained 'well balanced' schemes which properly treat the source term induced by a tapered artery (Delestre and Lagrée 2012). The 1D model and the numerical solutions have been validated by *in vitro* experimental (Alastruey et al. 2011; Saito et al. 2011; Wang et al. 2012) or *in vivo* clinical data (Stettler et al. 1981; Olufsen et al. 2000; Steele et al. 2003; DeVault et al. 2008; Reymond et al. 2009; Reymond et al. 2011). But usually only one particular scheme was chosen in a study and no cross comparisons among the schemes can be found. Sherwin et al. (2003) presented a Taylor–Galerkin (FE) and a DG method. The results of the two methods agree very well in a test case of an idealized vessel implanted with a stent. But no further detailed comparisons were made. Moreover, their work considered an elastic arterial wall instead of a viscoelastic wall. In fact, the diffusive term induced by viscoelasticity needs careful treatment. To our knowledge, there are no discussions in the literature on the advantage/ drawback of each scheme for a viscoelastic model.

Our objective in this paper is to make a cross comparison of the four numerical integration schemes and to suggest the suitable conditions of application for each scheme. In general, we note that FD schemes are not flexible enough to treat complex computational geometries in high dimensions (2D or 3D). However, FD, FE and FV schemes of low order accuracy are in fact completely equivalent for 1D linear problems. But for problems with large nonlinearities, solutions with sharp gradient may appear and the performances of different schemes could be different. Equally important is the numerical accuracy. For the DG scheme it may be tuned either by the degree of the polynomial or by the mesh size. But if a diffusive term is added to the governing equations, the term will be hard to treat by an implicit time marching method (e.g. Crank– Nicolson) in the DG setting, thus the time step may be very severely limited. Therefore, the performance of each scheme depends on the main features of the studied problems. In fact, problems with different main features arise in a wide range of applications. For instance, no shock is observed in arteries in normal physiological

conditions but shock-like phenomena may arise in veins (Brook et al. 1999; Marchandise and Flaud 2010; Flaud et al. 2012) or in arteries when the human body suffers from a blunt impact by accident (Kivity and Collins 1974). For another instance, in some conditions diffusive terms or dispersive terms may arise as source terms (Alastruey et al. 2011) and the proper treatment of these terms will pose different levels of difficulty in each numerical framework. Thus to make a cross comparison of the numerical schemes is interesting and useful.

In this paper, Section 2 presents the governing equations and the characteristic structure of the homo- geneous part of the nonlinear system. Section 3 describes the numerical solvers. In particular, a large amount of detail of computation is given because this kind of information is scattered in the literature. In this section, first an operator splitting is proposed (in the FD, FV and FE frameworks) to separate the hyperbolic and parabolic parts. Then the treatment of the BCs is discussed. Following that, MacCormack, Taylor–Galerkin and monotonic upwind scheme for conservation law (MUSCL) schemes are presented to integrate the hyperbolic subproblem. The parabolic subproblem is treated by a Crank–Nicolson method. At the end of this section, a local DG method is presented for the hyperbolic–parabolic problem without splitting. Section 4 shows the analytical solutions and numerical results of the proposed schemes. The system is linearized and asymptotic solutions are obtained with different source terms in the system. The effects of skin friction and viscosity of the wall on the pulse wave are clearly observed. Moreover, a wave with a step jump is computed and the ability of the four schemes to properly capture the shock-like phenomena is tested. After that, a simple bifurcation is computed and the numerical reflection and transmission coefficients are compared with the analytical coefficients predicted using linearized equations. Finally, a network with 55 arteries is computed. All the numerical solutions are compared favorably with the analytical, semi-analytical solutions or clinical observations. In the last section, comparisons among the four schemes are made in four important aspects: accuracy, ability to capture shock-like phenomena, computational speed and implementation complexity. The suitable conditions for the application of each scheme are discussed.

2. The 1D model of arterial blood flow

2.1 1D mathematical model

The details of the derivation of the 1D model can be found in the literature, such as Barnard et al. (1966), Formaggia et al. (2009), Hughes and Lubliner (1973) and Lagrée (2000). We stress the two main assumptions usually held in most applications: axisymmetric velocity profile and

large wavelength compared with the radius of the vessel. The 1D arterial blood flow model can be written as:

$$\frac{\partial A}{\partial t} + \frac{\partial Q}{\partial x} = 0, \tag{1a}$$

$$\frac{\partial Q}{\partial t} + \frac{\partial}{\partial x}\left(\alpha \frac{Q^2}{A}\right) + \frac{A}{\rho}\frac{\partial P}{\partial x} = -C_f \frac{Q}{A}, \tag{1b}$$

where, as stated above, A is the cross-sectional area of the artery, Q the volumetric flow rate or flux and P the internal pressure. The blood density ρ is assumed a constant. The independent variable t represents time and x the axial distance. Coefficient α is the momentum correction factor, and C_f is the skin friction coefficient. They depend on the shape of the velocity profile. Usually, the profile can be estimated from the Womersley number which is defined as $R\sqrt{\omega/\nu}$, with R being the radius of the vessel, ω the angular frequency of the pulse wave and ν the kinematic viscosity of the fluid. With a small Womersley number, we can take a Poiseuille (parabolic) profile. In that case $\alpha = 4/3$ and $C_f = 8\pi\nu$. This choice is only valid for very viscous flows (Lagrée and Rossi 1996; Lagrée 2000). In practice, viscosity is not so large, and the profile is more flat. For a completely flat profile α equals 1. This value is often used since it leads to a considerable simplification in analysis and the loss of relevance of the model is very small in most cases (Formaggia et al. 2003). Thus we assume its value is 1 in this paper. The value of C_f needs special attention because it has significant influence on the pulse wave. In practical applications, its value has to be determined according to the particular problem at hand (both *in vitro* and *in vivo* ones). We assume its value is $8\pi\nu$ according to a Poiseuille profile. We are aware of the limit of this approximation. However, as our purpose is comparison of numerical schemes, we do not discuss the values of α and C_f any more.

To close the system, several viscoelastic constitutive relations for arterial wall have been presented in the literature, such as Alastruey et al. (2011), Armentano et al. (1995), Holenstein et al. (1980) and Raghu et al. (2011). We choose the Kelvin–Voigt model for simplicity (Armentano et al. 1995; Alastruey et al. 2011). We assume that the arterial wall is thin, isotropic, homogeneous, incompressible, and moreover that it deforms axisymmetrically with each circular cross-section independently of the others. We denote the undeformed cross-sectional area by A_0 and the external pressure of the vessel by P_{ext}. Then, the relation linking A and P is

$$P = P_{\text{ext}} + \beta\left(\sqrt{A} - \sqrt{A_0}\right) + \nu_s \frac{\partial A}{\partial t}, \tag{2}$$

where the stiffness coefficient β is given as

$$\beta = \frac{\sqrt{\pi}Eh}{(1 - \eta^2)A_0},$$

and the viscosity coefficient ν_s as

$$\nu_s = \frac{\sqrt{\pi}\phi h}{2(1 - \eta^2)\sqrt{A_0}A}, \tag{3}$$

where η is the Poisson ratio, which is 0.5 for an incompressible material, E Young's modulus, h the thickness of the wall and ϕ the viscosity of the material. For convenience, we further define $C_{\text{v}} = A\nu_s/\rho$ for reasons which will be clear very soon in the next section. We also note that in the absence of the wall viscosity we retrieve the classical Hooke's law.

2.2 Characteristic structure of the system

After presenting the system of equations, we remind its hyperbolic feature by discussing the characteristic structure. The discussion is classical, and can be found in text books (LeVeque 2002; Formaggia et al. 2009). The notations we introduce here will be useful for the discussion of the numerical solvers. We assume P_{ext} is constant along the axial variable x, and substitute the constitutive relation (2) into Equation (1). We note that $\partial A/\partial t$ can be replaced by $-(\partial Q/\partial x)$, thanks to Equation (1). The equation for the balance of momentum turns out to

$$\frac{\partial Q}{\partial t} + \frac{\partial}{\partial x}\left(\frac{Q^2}{A} + \frac{\beta}{3\rho}A^{3/2}\right) - \frac{A}{\rho}\frac{\partial}{\partial x}\left(\nu_s \frac{\partial Q}{\partial x}\right)$$

$$= -C_f \frac{Q}{A} + \frac{A}{\rho}\left(\frac{\partial(\beta\sqrt{A_0})}{\partial x} - \frac{2}{3}\sqrt{A}\frac{\partial \beta}{\partial x}\right). \tag{4}$$

Under the assumption of a small perturbation of A, we approximate the term $(A/\rho)(\partial/\partial x)(\nu_s(\partial Q/\partial x))$ by $C_v(\partial^2 Q/\partial x^2)$ with the already defined coefficient $C_v = A\nu_s/\rho = (\sqrt{\pi}\phi h/(2\rho(1 - \eta^2)\sqrt{A_0}))$, which turns out to be independent of A or Q. The governing equations may be written as

$$\frac{\partial U}{\partial t} + \frac{\partial F}{\partial x} = S, \tag{5}$$

where

$$U = \begin{pmatrix} A \\ Q \end{pmatrix},$$

$$F = F_c + F_\nu = \begin{pmatrix} Q \\ \frac{Q^2}{A} + \frac{\beta}{3\rho}A^{3/2} \end{pmatrix} + \begin{pmatrix} 0 \\ -C_\nu \frac{\partial Q}{\partial x} \end{pmatrix},$$

and

$$S = \begin{pmatrix} 0 \\ -C_f \frac{Q}{A} + \frac{A}{\rho}\left(\frac{\partial(\beta\sqrt{A_0})}{\partial x} - \frac{2}{3}\sqrt{A}\frac{\partial\beta}{\partial x} \right) \end{pmatrix}.$$

In this equation, U is the conservative variable, F the corresponding flux and S the source term. Note that the flux (scaled by constant density) consists of two parts, the convective F_c and the diffusive F_v. We recognize Q^2/A due to fluid flow, $(\beta/3\rho)A^{3/2}$ due to elasticity, and $-C_v(\partial Q/\partial x)$ due to viscosity of the wall. In general, the suitable numerical techniques for the convective and diffusive fluxes are different. Thus it is common to separate the diffusive term and put it on the right side. Thus we may write the problem in a convection–diffusion form:

$$\frac{\partial U}{\partial t} + \frac{\partial F}{\partial x} = S + D, \tag{6}$$

with

$$F = F_c, \quad D = \begin{pmatrix} 0 \\ C_v \frac{\partial^2 Q}{\partial x^2} \end{pmatrix}.$$

We consider first the homogeneous part and later the non-homogeneous part. Expanding the derivative of the flux, the homogeneous part can be written in a quasi-linear form

$$\frac{\partial U}{\partial t} + J_c \frac{\partial U}{\partial x} = 0, \tag{7}$$

where J_c is the Jacobian matrix

$$J_c = \begin{pmatrix} 0 & 1 \\ \frac{Q^2}{A^2} + c^2 & 2\frac{Q}{A} \end{pmatrix},$$

with the Moens–Korteweg celerity

$$c = \sqrt{\frac{\beta}{2\rho}A^{1/2}}. \tag{8}$$

Actually, A is always positive. Therefore c is real, which is the speed of the pressure wave with respect to the fluid flow. Matrix J_c has two different eigenvalues

$$\lambda_{1,2} = \frac{Q}{A} \pm c. \tag{9}$$

Linear algebra shows J_c must be diagonalizable in the form $J_c = R\Lambda R^{-1}$. The columns of R are the right eigenvectors of J_c. Left multiplying Equation (7) by R^{-1}, and introducing a new vector W which satisfies $\partial_U W = R^{-1}$, one obtains

$$\frac{\partial W}{\partial t} + \Lambda \frac{\partial W}{\partial x} = 0. \tag{10}$$

$W_{1,2}$ can be readily obtained by integrating $\partial_U W = R^{-1}$ component-wise

$$W_{1,2} = \frac{Q}{A} \pm 4c. \tag{11}$$

$W = [W_1, W_2]^{\mathrm{T}}$ is called Riemann invariant vector or characteristics. In time–space plane, $W_{1,2}$ are constants along the lines $D_t X_{1,2}(t) = \lambda_{1,2}$. In physiological conditions, $\lambda_1 > 0 > \lambda_2$. The two families of characteristics propagate in opposite directions. The homogeneous part is a subcritical hyperbolic system. For further use, we get the expressions for A and Q by inverting relation (11),

$$A = \frac{(W_1 - W_2)^4}{1024}\left(\frac{\rho}{\beta}\right)^2, \quad Q = A\frac{W_1 + W_2}{2}. \tag{12}$$

In the non-homogeneous part, the skin friction term dissipates the momentum and the second-order derivative of Q is diffusive. Thus the full system has hyperbolic–parabolic features. In physiological conditions, the Womersley number is not too big and the artery is almost uniform, thus the source term will be very small and the system is dominated by the hyperbolicity feature. If the properties of the artery have sharp variations, large source terms will be introduced. In this case, we will treat the artery as different segments connected together.

3. Numerical solvers

Having defined the problem and notations, in this section we present the numerical solvers. The original problem is split into two subproblems which are, respectively, hyperbolic and parabolic. Three numerical schemes are presented to treat the hyperbolic subproblem. For the parabolic subproblem, Crank–Nicolson method is suitable. Because of the duplication of values at the interfaces of elements in the DG setting, there are difficulties in applying the Crank–Nicolson scheme. A local DG method is adopted to treat the problem without splitting.

3.1 Operator splitting

There are explicit high-resolution schemes for hyperbolic problems. But for parabolic problems, implicit schemes are necessary in general for a reasonable time step for time integration. Thus we applied a fractional step or operator splitting method. Starting from Equation (6), the original problem is split into to a hyperbolic subproblem,

$$\frac{\partial U}{\partial t} + \frac{\partial F}{\partial x} = S, \tag{13}$$

and a parabolic subproblem,

$$\frac{\partial U}{\partial t} = D. \tag{14}$$

Let us consider the time intervals (t^n, t^{n+1}), for $n = 0, 1, \ldots$ with $t^n = n\Delta t$. In every time interval, the hyperbolic problem is solved to get a predictor U^*, which is used as the initial condition (IC) of the second problem. The second step can be viewed as a corrector. The original problem is approximated by a sequential application of the two subproblems in a certain order.

From data U^n, we may make a prediction U^* by evolving time Δt of the hyperbolic subproblem, and correct it with the evolution over Δt of the parabolic subproblem,

$$U^n \xrightarrow{\mathrm{e}^{\Delta t \mathcal{H}}} U^* \xrightarrow{\mathrm{e}^{\Delta t \mathcal{P}}} U^{n+1},$$

where $\mathrm{e}^{\Delta t \mathcal{H}}(\mathrm{e}^{\Delta t \mathcal{P}})$ means to solve the hyperbolic (parabolic) subproblem over Δt. This method is called Godunov splitting. If the two subproblems are not commutable, the splitting error is $\mathcal{O}(\Delta t)$, see chapter 17 of LeVeque (2002).

There is a three-stage splitting called Strang splitting, which has a leading error term $\mathcal{O}(\Delta t^2)$,

$$U^n \xrightarrow{\mathrm{e}^{1/2\Delta t \mathcal{P}}} U^* \xrightarrow{\mathrm{e}^{\Delta t \mathcal{H}}} U^{**} \xrightarrow{\mathrm{e}^{1/2\Delta t \mathcal{P}}} U^{n+1}.$$

But in most cases the errors induced by the two splittings are very close. That is because the coefficient of the term $\mathcal{O}(\Delta t)$ is much smaller than the coefficient of $\mathcal{O}(\Delta t^2)$ (LeVeque 2002). We will see in Section 4.3 a test case on the diffusion term. The results show that Godunov splitting is sufficient for our problem.

Because the system is dominated by the hyperbolicity, it must be driven mainly by the BCs through the first subproblem. Thus we discuss the BC of the hyperbolic part in the next subsection and present the treatment of BC for the parabolic part in Section 3.6 together with Crank–Nicolson scheme.

3.2 IC and BC

3.2.1 Initial conditions

Assume we are interested in the blood flow in an arterial segment $(0, L)$ within a time interval $(0, T)$. For an evolutionary problem, a proper IC is needed. In reality, the information contained in IC flows out after a certain interval of time, and it will not have an influence on the system thereafter. Thus, the IC can be set arbitrarily, say, $U(t = 0, x) = (A_0, 0)$, for convenience.

3.2.2 Inlet and outlet of the homogeneous hyperbolic part

Assuming the source terms are small, we can impose the BC approximately by taking advantage of the characteristic structure of the homogeneous part (Formaggia et al. 2003). Let us look back to the vector equation (10) again. The two components of this system are

$$\frac{\partial W_1}{\partial t} + \lambda_1 \frac{\partial W_1}{\partial x}(U) = 0, \tag{15a}$$

$$\frac{\partial W_2}{\partial t} + \lambda_2 \frac{\partial W_2}{\partial x}(U) = 0. \tag{15b}$$

Since the two eigenvalues have opposite signs, there is exactly one incoming characteristic at each end of the computational domain. The incoming characteristic carries information from outside of the domain and thus is essential to guarantee the problem to be well posed. That is to say, the system must be supplemented by BCs in the form

$$W_1(0, t) = g_1(t), \quad W_2(L, t) = g_2(t), \quad t > 0. \tag{16}$$

The outgoing characteristic carries information from inside of the domain, which can be given by the differential equations. Since $W_{1,2}$ are constants along the lines $D_t X_{1,2}(t) = \lambda_{1,2}$ in time–space plane, we can get $W_2^{n+1}(0)$ and $W_1^{n+1}(L)$ by interpolation in the data of the n-th time step:

$$\begin{aligned} W_2^{n+1}(0) &= W_2^n\big(-\lambda_2^n(0)\Delta t\big), \\ W_1^{n+1}(L) &= W_1^n\big(L - \lambda_1^n(L)\Delta t\big). \end{aligned} \tag{17}$$

The characteristics are then transformed to physical variables by relation (12) for numerical computation.

In reality, we rarely have the explicit expression (16) for the incoming characteristics. Usually, we want to impose BC in physical term A, Q or P. At the inlet, if A^{n+1} is given, one can use relation (11) to deduce

$$W_1^{n+1} = W_2^{n+1} + 8\sqrt{\frac{\beta}{2\rho}}\sqrt{A^{n+1}}.$$

If Q^{n+1} is given, we approximate A^{n+1} by A^n and then obtain

$$W_1^{n+1} = -W_2^{n+1} + 2\frac{Q^{n+1}}{A^n}.$$

If P^{n+1} is given, from the wall relation (2) simplified with no viscous effect ($\nu_s = 0$), we in fact impose

$$W_1^{n+1} = W_2^{n+1} + 8\sqrt{\frac{1}{2\rho}\big(P^{n+1} + \beta A_0^{1/2}\big)}.$$

At the outlet, some part of the perturbation of outgoing characteristic W_1 may be reflected,

$$W_2^{n+1} = W_2^0 - R_t\left(W_1^{n+1} - W_1^0\right),$$

where R_t is the coefficient of reflection. If $R_t = 0$, the BC is non-reflecting. That means the outgoing characteristic goes out without leaving any effect and that the incoming characteristic is a constant in time. If there are changes of properties in the downstream of the vessel, usually a non-zero R_t will be incurred.

3.2.3   Conjunction points

There are many cases when conjunctions of different vessels need to be considered: when there are changes of topology, sharp variations in geometrical or mechanical properties. Topological changes correspond to the large amount of bifurcations and some trifurcations in the arterial network. Sharp variations may also arise in many conditions, for example when there are increases of stiffness β due to stenting or A_0 due to aneurysm. In these cases, the derivatives of the corresponding variables in the source terms are very large or even near a singularity, and then the vessel can be treated as several joined segments with different properties.

Since all of the conjunction points can be treated with the same method, we consider a branching point as a sample problem: a parent vessel with two daughter arteries. At the branching point, there are then six BCs, A_p^{n+1} and Q_p^{n+1} for the outlet of the parent artery and $A_{d_1}^{n+1}$, $Q_{d_1}^{n+1}$, $A_{d_2}^{n+1}$ and $Q_{d_2}^{n+1}$ for the inlets of the two daughter arteries. From the physical point of view, we have to preserve the conservation of mass flux

$$Q_p^{n+1} - Q_{d_1}^{n+1} - Q_{d_2}^{n+1} = 0, \qquad (18a)$$

and conservation of momentum flux

$$\frac{1}{2}\rho\left(\frac{Q_p^{n+1}}{A_p^{n+1}}\right)^2 + P_p^{n+1} - \frac{1}{2}\rho\left(\frac{Q_{d_i}^{n+1}}{A_{d_i}^{n+1}}\right)^2 - P_{d_i}^{n+1} = 0, \qquad (18b)$$

$$i = 1, 2.$$

Pressures P_p^{n+1} and $P_{d_i}^{n+1}$ shall be expressed in cross-sectional area A by the constitutive relation (2). In Equation (18b), there may be some terms for energy losses due to branching (Formaggia et al. 2003; Steele et al. 2003; Matthys et al. 2007). But in practice, these losses only have secondary effects on the pulse waves (Matthys et al. 2007). Therefore, we did not include them.

Moreover, the outgoing characteristics of the joined arteries should be matched. In the parent artery, $(W_1)_p^{n+1}$ is given by the data on the n-th time step with the

interpolation formula (17). It must be equal to $W_1(U_p^{n+1})$ which is given by relation (11). Thus we have the equation

$$(W_1)_p^{n+1} - W_1\left(U_p^{n+1}\right) = 0. \qquad (18c)$$

The same principle holds for W_2 on the two daughter arteries,

$$(W_2)_{d_i}^{n+1} - W_2\left(U_{d_i}^{n+1}\right) = 0, \quad i = 1, 2. \qquad (18d)$$

Combining Equations (18a)–(18d), there are six equations with six unknowns. This nonlinear algebraic system can be readily solved by Newton–Raphson iterative method with U^n as the initial guess. In our test, the computation converges very fast. Usually a very few iterations are enough for a satisfactory accuracy.

3.3   MacCormack scheme

In FD framework, MacCormack method (MacCormack 2003) is very suitable for nonlinear hyperbolic systems of conservation laws. It is equivalent to the Lax–Wendroff scheme for linear systems. It has the following characteristics: conservative form, three-point spatial stencil and two time levels (predictor and corrector), second-order accuracy in time and space.

The numerical solution is performed in a mesh with $N + 1$ points and thus the spatial resolution is $\Delta x = L/N$, see Figure 1. For the conservative system (13), an approximate solution $\mathbf{U}^*$ is obtained first from $\mathbf{U}^n$ and then $\mathbf{U}^*$ is corrected to give the solution $\mathbf{U}^{n+1}$ at the time step $t + \Delta t$. The FD equations (at the interior grid points) are then:

1. Predictor step:

$$U_i^* = U_i^n - \frac{\Delta t}{\Delta x}\left(F_{i+1}^n - F_i^n\right) + \Delta t S_i^n,$$

$$i = 2, \ldots, N,$$

2. Corrector step:

$$U_i^{n+1} = \frac{1}{2}\left(U_i^n + U_i^*\right) - \frac{\Delta t}{2\Delta x}\left(F_i^* - F_{i-1}^*\right) + \frac{\Delta t}{2}S_i^*,$$
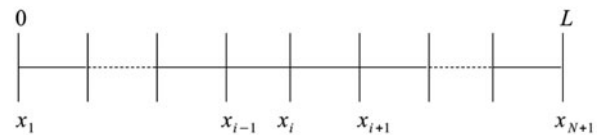$$i = 2, \ldots, N,$$

Figure 1.   Mesh for FD and FE.

where $\mathbf{F}^*$ and $\mathbf{S}^*$ are evaluated as functions of the predicted solution $\mathbf{U}^*$. Note that the predictor step applies a forward differencing and the corrector step a backward differencing. The order of the two kinds of differencing can be reversed. The grid points x_1 and x_{N+1} represent the BCs.

3.4 Taylor–Galerkin scheme

In this section, we follow the presentations of Formaggia et al. (2003, 2009) and Sherwin et al. (2003) for the Taylor–Galerkin scheme. Other forms are also possible, see Wan et al. (2002), for example.

From Equation (13), one may obtain

$$\frac{\partial U^n}{\partial t} = S^n - \frac{\partial F^n}{\partial x}. \tag{19}$$

Differentiating both sides with respect to t and exchanging the order of spatial and temporal differentiations in the second term give

$$\frac{\partial^2 U^n}{\partial t^2} = \left(S_U \frac{\partial U}{\partial t}\right)^n - \frac{\partial}{\partial x}\left(H \frac{\partial U}{\partial t}\right)^n, \tag{20}$$

where $S_U = \partial S / \partial U$ and $H = \partial F / \partial U$. Substituting Equation (19) into Equation (20) and then both of them into the Taylor series of U^{n+1} up to the second order, one gets

$$\begin{aligned}
U^{n+1} = U^n &- \Delta t \frac{\partial}{\partial x}\left[F^n + \frac{\Delta t}{2} H^n S^n\right] \\
&- \frac{\Delta t^2}{2}\left[S_U^n \frac{\partial F^n}{\partial x} - \frac{\partial}{\partial x}\left(H^n \frac{\partial F^n}{\partial x}\right)\right] \\
&+ \Delta t \left(S^n + \frac{\Delta t}{2} S_U^n S^n\right).
\end{aligned} \tag{21}$$

For convenience, we adopt the notations

$$F_{LW}(U) = F(U) + \frac{\Delta t}{2} H(U) S(U),$$

$$S_{LW}(U) = S(U) + \frac{\Delta t}{2} S_U(U) S(U).$$

The piecewise linear function space associated with the mesh (Figure 1) is given as

$$V_h^0 = \big\{[v_h]^2 | v_h \in \mathcal{C}^0, v_h|_{[x_i, x_{i+1}]} \in \mathcal{C}^1,$$
$$v_h(0) = v_h(L) = 0, \ i = 1, \dots, N\big\}.$$

This is both the trial function space and the test function space in the Galerkin framework. We further define the inner product

$$(U, V) = \int_0^L U \cdot V \, \mathrm{d}x.$$

At the interior points $x_2, \dots, x_N$, if we approximate U by $U_h \in V_h^0$ in Equation (21), multiply both sides by basis test functions $\psi_i \in V_h^0$, and integrate over the domain $[0, L]$, finally we can get

$$\begin{aligned}
\left(U_h^{n+1}, \psi_i\right) = &\left(U_h^n, \psi_i\right) + \Delta t \left(F_{LW}\left(U_h^n\right), \frac{\mathrm{d}\psi_i}{\mathrm{d}x}\right) \\
&- \frac{\Delta t^2}{2}\left(S_U\left(U_h^n\right) \frac{\partial F\left(U_h^n\right)}{\partial x}, \psi_i\right) \\
&- \frac{\Delta t^2}{2}\left(H\left(U_h^n\right) \frac{\partial F\left(U_h^n\right)}{\partial x}, \frac{\mathrm{d}\psi_i}{\mathrm{d}x}\right) \\
&+ \Delta t \left(S_{LW}\left(U_h^n\right), \psi_i\right).
\end{aligned} \tag{22}$$

In computation, we enforce Equation (22) component-wise. That is,

$$\left(A_h^{n+1}, v_i\right) = RHS1_i^n, \quad \left(Q_h^{n+1}, v_i\right) = RHS2_i^n,$$

where v_i is one component of vector ψ_i and

$$\begin{aligned}
RHS1_i^n = &\left(A_h^n, v_i\right) + \Delta t \left(\left[F_{LW}\left(U_h^n\right)\right]_1, \frac{\mathrm{d}v_i}{\mathrm{d}x}\right) \\
&- \frac{\Delta t^2}{2}\left(\left[S_U\left(U_h^n\right) \frac{\partial F\left(U_h^n\right)}{\partial x}\right]_1, v_i\right) \\
&- \frac{\Delta t^2}{2}\left(\left[H\left(U_h^n\right) \frac{\partial F\left(U_h^n\right)}{\partial x}\right]_1, \frac{\mathrm{d}v_i}{\mathrm{d}x}\right) \\
&+ \Delta t \left(\left[S_{LW}\left(U_h^n\right)\right]_1, v_i\right).
\end{aligned} \tag{23}$$

Form $[\cdot]_1$ indicates the first component of the vector in the bracket. $RHS2_i^n$ can be expressed in a similar way.

To elaborate the computing details, we take Equation (23) as an example. In the FE framework, A_h^{n+1} and A_h^n are expanded as $A_h = \sum_{j=2}^{j=N} A_j v_j$. We denote the unknown vector $(A_2, \dots, A_N)^{\mathrm{T}}$ by $\mathbf{A}$. Instead of evaluated directly as nonlinear functions of U_h^n, terms $F(U_h^n)$, $F_{LW}(U_h^n)$, $S_{LW}(U_h^n)$, $S_U(U_h^n)$ and $H(U_h^n)$ are projected onto the trial function space and expanded by a group FE method. That is, for example $[F(U_h^n)]_1 = \sum_{j=2}^{j=N} [F_j^n]_1 v_j$ with $[F_j^n]_1 = [F(U_j^n)]_1$. Finally, the matrix form of Equation (23) writes

$$\begin{aligned}
\mathcal{M} \mathbf{A}^{n+1} = &\mathcal{M} \mathbf{A}^n + \Delta t \mathcal{K}^T \left[\mathbf{F}_{LW}^n\right]_1 \\
&- \frac{\Delta t^2}{2} (\tilde{\mathcal{M}}_1 [\mathbf{F}^n]_1 + \tilde{\mathcal{M}}_2 [\mathbf{F}^n]_2) \\
&- \frac{\Delta t^2}{2} (\tilde{\mathcal{K}}_1 [\mathbf{F}^n]_1 + \tilde{\mathcal{K}}_2 [\mathbf{F}^n]_2) \\
&+ \Delta t \mathcal{M} \left[\mathbf{S}_{LW}^n\right]_1,
\end{aligned} \tag{24}$$

where

$$\mathcal{M}_{ij} = (v_i, v_j), \quad \mathcal{K}_{ij} = \left(v_i, \frac{\partial v_j}{\partial x}\right),$$

and

$$\tilde{\mathcal{M}}_1(S_u)_{ij} = \left(\sum_k \left(S_u^{(1,1)}\right)_k v_k \frac{\partial v_i}{\partial x}, v_j\right),$$

$$\tilde{\mathcal{M}}_2(S_u)_{ij} = \left(\sum_k \left(S_u^{(1,2)}\right)_k v_k \frac{\partial v_i}{\partial x}, v_j\right),$$

$$\tilde{\mathcal{K}}_1(H)_{ij} = \left(\sum_k H_k^{(1,1)} v_k \frac{\partial v_i}{\partial x}, \frac{\partial v_j}{\partial x}\right),$$

$$\tilde{\mathcal{K}}_2(H)_{ij} = \left(\sum_k H_k^{(1,2)} v_k \frac{\partial v_i}{\partial x}, \frac{\partial v_j}{\partial x}\right).$$

Form $\left(S_u^{(\cdot,\cdot)}\right)_k$ indicates the k-th component of the vector at position $(\cdot,\cdot)$ of the discretized matrix $\mathbf{S}_u$. Please note that operators $\tilde{\mathcal{M}}_1$, etc. are functions of $\mathbf{S}_u$ and $\mathbf{H}$, therefore they must be updated in every time step.

3.5   Monotonic upwind scheme for conservation law

In this section, we mainly follow presentation (Delestre and Lagrée 2012) but with a different temporal integration method. For FV method, the domain is decomposed into FVs or cells with vertex x_i as the center of cell $[x_{i-1/2}, x_{i+1/2}]$, see Figure 2. In each cell, average values are considered,

$$U_i = \frac{1}{\Delta x} \int_{x_{i-1/2}}^{x_{i+1/2}} U(x)\mathrm{d}x, \quad S_i = \frac{1}{\Delta x} \int_{x_{i-1/2}}^{x_{i+1/2}} S(x)\mathrm{d}x.$$

Integrating the governing equations over each cell and applying Gauss's theorem, one readily obtains

$$\frac{\mathrm{d}U_i}{\mathrm{d}t} = -\frac{(F|_{x_{i+1/2}} - F|_{x_{i-1/2}})}{\Delta x} + S_i. \tag{25}$$

We have a local Riemann problem at each interface of neighboring cells, since $U_{i+1/2-}$ and $U_{i+1/2+}$, the left limit of U_i and the right limit of U_{i+1} at $x_{i+1/2}$, respectively, are not equal in general. By solving the Riemann problem, a numerical flux F^* can be obtained. Depending on the
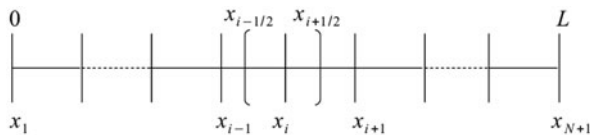

Figure 2.   Mesh for FV.

approximate approaches on solving the Riemann problem, different numerical fluxes are possible. Among them, Rusanov (or called local Lax–Friedrichs) flux is widely used. According to Bouchut (2004), it writes

$$F_{i+1/2}^* = \frac{F(U_{i+1/2-}) + F(U_{i+1/2+})}{2}$$
$$- c\frac{U_{i+1/2+} - U_{i+1/2-}}{2},$$

with

$$c = \max(\lambda_1(U_{i+1/2-}), \lambda_1(U_{i+1/2+})),$$

where λ_1 is the biggest eigenvalue of J_c. Other numerical fluxes with less numerical diffusivity are possible, such as Harten-Lax-van Leer (HLL) flux (Bouchut 2004; Delestre and Lagrée 2012). Since Rusanov flux is more simple and robust, it is adopted in this paper. If $\mathbf{U}_-$ and $\mathbf{U}_+$ are equal to the average values at the cells, the scheme will be of first-order accuracy. Reconstructions of $\mathbf{U}_-$ and $\mathbf{U}_+$ from $\mathbf{U}$ are necessary for a scheme of higher resolution.

Let us consider the techniques of reconstruction. For a scalar s within the i-th cell, we denote its slope as Ds_i, which can be approximated by $(s_i - s_{i-1})/\Delta x$, $(s_{i+1} - s_i)/\Delta x$ or $(s_{i+1} - s_{i-1})/2\Delta x$. Then the values of s at the interfaces associated with this cell can be recovered as

$$s_{i-1/2+} = s_i - \frac{\Delta x}{2}Ds_i, \quad s_{i+1/2-} = s_i + \frac{\Delta x}{2}Ds_i.$$

The discretization of derivative in space can achieve a second-order accuracy by this method. But the solution will have non-physical oscillations. Some examples of oscillations induced by these methods can be found in Chapter 6 of LeVeque (2002). Slope or flux limiter and non-oscillatory solutions are integral characteristics of FV schemes. MUSCL is one popular slope-limited linear reconstruction technique. To present MUSCL, we first define a slope limiter

$$\mathrm{minmod}(x, y) = \begin{cases} \min(x, y) & \text{if } x, y \geq 0, \\ \max(x, y) & \text{if } x, y \leq 0, \\ 0 & \text{else.} \end{cases}$$

Then slope Ds_i is modified as

$$Ds_i = \mathrm{minmod}\left(\frac{s_i - s_{i-1}}{\Delta x}, \frac{s_{i+1} - s_i}{\Delta x}\right).$$

The values of $\mathbf{U}_-$ and $\mathbf{U}_+$ at the interfaces can be obtained by linear reconstruction with slope Ds_i. The variables are conserved by this reconstruction.

After the discretization in space, we have the semi-discrete form,

$$\frac{dU_i}{dt} = \Phi(U_{i-2}, \ldots, U_{i+2}),$$

where

$$\Phi(U_{i-2}, \ldots, U_{i+2}) = -\frac{\left(F^*_{i+1/2} - F^*_{i-1/2}\right)}{\Delta x} + S_i.$$

Numerical fluxes $F^*_{i+1/2}$ and $F^*_{i-1/2}$ are given by Rusanov flux with the reconstructed values at the two sides of the interfaces. Note that this is a scheme with five stencils. The values at x_1 and x_{N+1} are determined by the aforementioned characteristic method. One ghost cell at each end of the computational domain is needed and we approximate the values at these cells by those at the neighboring boundary cells.

For the temporal integration, we may apply a two-step second-order Adams–Bashforth (A–B) scheme,

$$\mathbf{U}^{n+1} = \mathbf{U}^n + \Delta t\left(\frac{3}{2}\Phi(\mathbf{U}^n) - \frac{1}{2}\Phi(\mathbf{U}^{n-1})\right).$$

This scheme can be initiated by a forward Euler method. Also, a second-order Runge–Kutta (R–K) approach, namely Heun method, is possible (Shu and Osher 1988). It is written as

$$\mathbf{U}^* = \mathbf{U}^n + \Delta t\Phi(\mathbf{U}^n),$$
$$\mathbf{U}^{**} = \mathbf{U}^* + \Delta t\Phi(\mathbf{U}^*),$$
$$\mathbf{U}^{n+1} = (\mathbf{U}^* + \mathbf{U}^{**})/2.$$

Comparing the two methods, we note that $\Phi(\mathbf{U})$ has to be computed twice in R–K in every time step while the A–B method only needs once since $\Phi(\mathbf{U}^{n-1})$ is stored in the previous step and reused in the current step. Because the BCs are determined dynamically to compute $\Phi(\mathbf{U})$, the R–K also incurs one more resolution of the nonlinear algebraic equations at conjunction points. For these reasons, we choose the A–B method for the temporal integration, although the R–K method usually allows a larger time step for convergence.

3.6 Treatment of the parabolic subproblem

For the previous three schemes, only the hyperbolic subproblem resulted from splitting is solved. For the parabolic subproblem, the Crank–Nicolson method is very suitable. The temporal and spatial discretization has the form

$$\frac{U_i^{n+1} - U_i^*}{\Delta t} = \frac{C_v}{2}\left(\frac{U_{i+1}^{n+1} - 2U_i^{n+1} + U_{i-1}^{n+1}}{\Delta x^2} + \frac{U_{i+1}^* - 2U_i^* + U_{i-1}^*}{\Delta x^2}\right),$$

where $\mathbf{U}^*$ is the solution of the first hyperbolic subproblem. The matrix of the resulting algebraic system is tridiagonal, which is quite cheap to invert. This scheme is second-order accurate both on time and space. Moreover, it is unconditionally stable. It is natural to set a homogeneous Neumann BC for the parabolic subproblem, $\partial_x U_p(0, t) = \partial_x U_p(L, t) = 0$. Subscript p stands for parabolic. We note that a second-order implicit FE method can also be applied here. But since this subproblem is linear and is in 1D, the FE method would be exactly equivalent to this FD method.

3.7 Local DG scheme

In the FV framework, the recovery of $\mathbf{U}_-$ and $\mathbf{U}_+$ of higher accuracy requires a big stencil. In higher dimensions, this kind of reconstruction leads to difficulties if the mesh is unstructured. On the other hand, it is quite straightforward to increase the order of approximation polynomials in one FE. Unlike the global FE, the neighboring elements do not share the same values at the interfaces. Numerical fluxes are obtained from these values, where the dynamics of the system can be considered. We present a nodal DG scheme, following Hesthaven and Warburton's book (Hesthaven and Warburton 2008). The domain is decomposed into K non-overlapping elements, see Figure 3. At each element, the local approximation to the solution is a polynomial of order $N = N_p - 1$. The global approximation to U is the direct summation of these local solutions:

$$U_h = \bigoplus_{k=1}^{k=K} U_h^k. \tag{26}$$

Similarly, flux F and the source term S can also be approximated by the direct summation of piecewise N-th degree polynomials. The local form of the conservation law on the k-th element is

$$\frac{\partial U_h^k}{\partial t} + \frac{\partial F_h^k}{\partial x} = S_h^k. \tag{27}$$
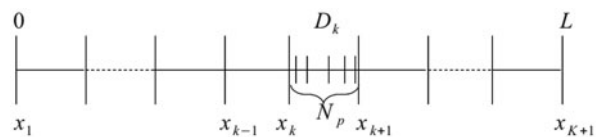

Figure 3. Mesh for DG.

Multiplying both sides of Equation (27) with a test function ψ^k and integrating over one element give

$$\left(\frac{\partial U_h^k}{\partial t}, \psi^k\right)_{D_k} + \left(\frac{\partial F_h^k}{\partial x}, \psi^k\right)_{D_k} = \left(S_h^k, \psi^k\right)_{D_k}. \quad (28)$$

Applying integration by parts on the second term, we have

$$\left(\frac{\partial U_h^k}{\partial t}, \psi^k\right)_{D_k} - \left(F_h^k, \frac{\partial \psi^k}{\partial x}\right)_{D_k} + F_h^k \psi^k|_{x_k}^{x_{k+1}}$$
$$= \left(S_h^k, \psi^k\right)_{D_k}. \quad (29)$$

At the interface of x_k, the values of U_h at the two sides, $U_h^{k-1}(x_k)$ and $U_h^k(x_k)$, are not guaranteed equal. A numerical flux F_k^* is introduced here. Through the numerical flux, information is communicated between elements. In practice, the second term is integrated by parts again for convenience of computation. Thus we have

$$\left(\frac{\partial U_h^k}{\partial t}, \psi^k\right)_{D_k} + \left(\frac{\partial F_h^k}{\partial x}, \psi^k\right)_{D_k} + \psi^k\left(-F_h^k + F^*\right)|_{x_k}^{x_{k+1}}$$
$$= \left(S_h^k, \psi^k\right)_{D_k}. \quad (30)$$

If we introduce N_p nodes within element D_k (Figure 3), the local solution can be expanded as

$$U_h^k(x, t) = \sum_{i=1}^{N_p} U_h^k(x_i^k, t) \ell_i^k(x), \quad (31)$$

where $\ell_i^k(x)$ is the Lagrange interpolant associated with the i-th node. For the Galerkin scheme, Equation (30) must hold for every test function $\ell_i^k(x)$. Thus we have N_p equations for N_p unknowns. In matrix form, the system can be written as

$$\mathcal{M}^k \frac{\mathrm{d}\mathbf{U}^k}{\mathrm{d}t} + \mathcal{K}^k \mathbf{F}^k + \ell^k\left(-F_h^k + F^*\right)\Big|_{x_k}^{x_{k+1}} = \mathcal{M}^k \mathbf{S}^k, \quad (32)$$

where

$$\mathcal{M}_{(i,j)}^k = \left(\ell_i^k, \ell_j^k\right)_{D_k}, \quad \mathcal{K}_{(i,j)}^k = \left(\ell_i^k, \frac{\mathrm{d}\ell_j^k}{\mathrm{d}x}\right)_{D_k},$$

and ℓ^k is the vector of functions $\left(\ell_1^k, \ell_2^k, \ldots, \ell_{N_p}^k\right)^{\mathrm{T}}$. The system of equations can be turned into a semi-discrete form

$$\frac{\mathrm{d}\mathbf{U}^k}{\mathrm{d}t} = -\mathcal{D}^k \mathbf{F}^k + (\mathcal{M}^k)^{-1}\ell^k\left(F_h^k - F^*\right)\Big|_{x_k}^{x_{k+1}} + \mathbf{S}^k, \quad (33)$$

where

$$\mathcal{D}_{(i,j)}^k = \left((\mathcal{M}^k)^{-1}\mathcal{K}^k\right)_{(i,j)} = \frac{\mathrm{d}\ell_j^k}{\mathrm{d}r}\Bigg|_{r_i}$$

is the local differentiation operator (Hesthaven and Warburton 2008). The computation of $\mathcal{M}^k$ and $\mathcal{D}^k$ is crucial. We define an affine mapping from a reference element $(-1, 1)$ to D_k,

$$x(r) = x_k + \frac{1 + r}{2}(x_{k+1} - x_k).$$

The local operators can be readily computed as

$$\mathcal{M}_{(i,j)}^k = \mathcal{J}_k \int_{-1}^1 \ell_i \ell_j \, \mathrm{d}r, \quad \mathcal{D}_{(i,j)}^k = \mathcal{J}_k^{-1} \frac{\mathrm{d}\ell_j}{\mathrm{d}r}\Bigg|_{r_i},$$

where $\mathcal{J}_k = (x_{k+1} - x_k)/2$ and ℓ_i and ℓ_j are the Lagrange interpolants at the reference element. Note that operators $\mathcal{M}^k$ and $\mathcal{D}^k$ can be precomputed and stored. Legendre–Gauss–Lobatto points have to be chosen as the interpolation points to minimize computation error. For more details, we refer to Chapter 3 of Hesthaven and Warburton (2008). For the temporal integration, a second-order A–B scheme is applied for reasons as discussed in Section 3.5.

The scheme previously presented can treat a hyperbolic problem. But in this setting the Crank–Nicolson method is hard to apply, because the values at the interfaces are duplicated. We consider the problem formulation of Equation (5), where the flux contains convective part F_c and diffusive part F_v. For the convective part, Rusanov flux as mentioned in Section 3.5 is applicable. For the diffusive flux, a straight idea is to use the central flux $(F_v(U_-) + F_v(U_+))/2$. But as pointed out by Shu (2001), this choice is inconsistent.

To solve this problem, we rewrite the original equations as

$$\frac{\partial U}{\partial t} + \frac{\partial(F_c - C_v q)}{\partial x} = S, \quad q - \frac{\partial Q}{\partial x} = 0.$$

In semi-discrete form, the equations for one element are

$$\frac{\mathrm{d}\mathbf{U}_k}{\mathrm{d}t} = -\mathcal{D}^k \mathbf{F}^k + (\mathcal{M}^k)^{-1}\ell^k\left(F_h^k - F^*\right)\Big|_{x_k}^{x_{k+1}} + \mathbf{S}^k,$$

$$\mathbf{q}^k = \mathcal{D}^k \mathbf{Q}^k - (\mathcal{M}^k)^{-1}\ell^k\left(Q_h^k - Q^*\right)\Big|_{x_k}^{x_{k+1}}.$$

The fluxes in these equations have to be modified accordingly: $\mathbf{F}^k = \mathbf{F}_c^k - C_v \mathbf{q}^k$, $F_h^k = (F_c)_h^k - C_v q_h^k$ and $F^* = F_c^* - (C_v q)^*$. The convective flux F_c^* is defined by Rusanov flux. Fluxes $(C_v q)^*$ and Q^* are defined by the central flux. The introduction of an auxiliary variable q stabilizes the scheme. Note that the auxiliary equation does not involve time evolution. The computation and

storage of q^k incurs very limited extra costs. This method is called the local DG scheme.

4. Results and discussion

The implementation codes can be verified by analytical solutions of linearized model or manufactured solutions of the full system without linearization (Raghu and Taylor 2011; Raghu et al. 2011). In this paper, except comparisons with the homogeneous linearized model and results in the literature, we derived asymptotic solutions with different source terms. The verification by asymptotic analysis is a different approach from previous work. In this section, the computations are done on a single uniform vessel at first. In case of small perturbations, a linearized system is obtained. If this system is homogeneous, it allows pure wave solution. If the source terms due to skin friction and viscosity of the wall are added, respectively, asymptotic solutions are obtained. In case of larger perturbations, the full nonlinear system allows shocks. The shock-capturing property of each scheme is tested in this case. After the tests on a single vessel, a simple bifurcation is computed and the reflection and transmission coefficients are compared with analytical coefficients predicted by the linearized system. At the end of this section, a network with 55 arteries is computed and the numerical solutions are checked against clinical observations reported in the literature.

4.1 Propagation in a uniform tube

In this subsection, we compare the numerical results with analytical results for a pulse wave on a single uniform vessel ($\partial_x(\beta\sqrt{A_0}) = \partial_x\beta = 0$). To avoid reflections, non-reflecting BC is set at the outflow to mimic a semi-infinite tube. Adding a small perturbation ($\epsilon\tilde{A}, \epsilon\tilde{Q}$) to the equilibrium solution ($U = (A_0, 0)$), substituting it into the governing equations and dropping the terms with quadratics of ϵ, we obtain the equations for the perturbations in a linear form:

$$\frac{\partial\tilde{A}}{\partial t} + \frac{\partial\tilde{Q}}{\partial x} = 0, \quad \frac{\partial\tilde{Q}}{\partial t} + c_0^2\frac{\partial\tilde{A}}{\partial x} = -\frac{C_f}{A_0}\tilde{Q} + C_v\frac{\partial^2\tilde{Q}}{\partial x^2}, \quad (34)$$

where $c_0 = \sqrt{(\beta/2\rho)}\sqrt{A_0}$, the Moens–Korteweg celerity. To investigate the propagation phenomena at first, we drop the non-homogeneous part ($C_f = 0$ and $C_v = 0$). Then Equation (34) become d'Alembert equations, which admit the pure wave solution. We assume that the IC is at equilibrium and the inflow is prescribed as $Q(0, t) = Q_{\text{in}}(t)$ with

$$Q_{\text{in}}(t) = Q_c\sin\left(\frac{2\pi}{T_c}t\right)H\left(-t + \frac{T_c}{2}\right), \quad t > 0,$$

where $H(t)$ is the Heaviside function, T_c the period of the sinusoidal wave and Q_c the amplitude. The solution is $c_0\tilde{A} = \tilde{Q} = Q_{\text{in}}(x - c_0t)$, which means that the waveform propagates to the right with a speed of c_0.

We propose a numerical test with parameters of the tube inspired by Sherwin et al. (2003): $L = 250$ cm, $A_0 = 3.2168$ cm^2, $\beta = 1.8734 \times 10^6$ Pa/m, $\rho = 1.050 \times 10^3$ kg/m^3 and accordingly $c_0 = 400$ cm/s. To impose a small perturbation, we choose $Q_c = 1$ ml/s and $T_c = 0.4$ s. In this case the change ratio of the radius is $\Delta R/R_0 = Q_c/(2A_0c_0) = 0.04\%$, thus the perturbation is assured small enough. We take the linearized analytical solution at time $t = 0.4$ s as reference to compute the errors of the numerical solutions. The normalized error is defined by $\|E\| = \|\mathbf{Q}_{\text{numerical}} - \mathbf{Q}_{\text{analytical}}\|_{\text{rms}}/Q_c$, where $\|\cdot\|_{\text{rms}}$ stands for the root-mean-square error. To specify the time step, we note that it first should satisfy the Courant–Friedrichs–Lewy (CFL) condition which is written as

$$\Delta t \leq n_{\text{CFL}}\min_{i=0}^{N+1}\left[\frac{h_i}{\max\left((Q_i/A_i) + c_i, (Q_{i+1}/A_{i+1}) + c_{i+1}\right)}\right],$$

where h_i is the element (cell) size. For the second-order Taylor–Galerkin scheme, a linear stability analysis shows that $n_{\text{CFL}} = \sqrt{3}/3$ (Formaggia et al. 2003). For the second-order MUSCL, $n_{\text{CFL}} = 1/2$ (Delestre and Lagrée 2012). Practice shows that $n_{\text{CFL}} = 1$ for the MacCormack scheme (Elad et al. 1991). A sharp estimation of coefficient n_{CFL} for the DG scheme is challenging. We define an approximate formula, $\Delta t = C_t(L/Nc_0)$, to test the stability. In our test, the approximate threshold values of C_t for the schemes to become unstable are 0.5 for MUSCL, 0.56 for Taylor–Galerkin and 1.0 for MacCormack. The results agree with the report in the literature. For the DG scheme, the time step formula is modified accordingly as $\Delta t = (C_t/\mathcal{P})(L/Nc_0)$, where $\mathcal{P}$ is the degree of the polynomial. For the DG scheme, C_t cannot be greater than 0.1 (Figure 4(b)).

To further test the temporal convergence, we fix the mesh ($N_{\text{TG}} = N_{\text{FV}} = N_{\text{FD}} = 800$, $N_{\text{DG-}\mathcal{P}_1} = N_{\text{DG-}\mathcal{P}_2} = 100$) and plot the numerical errors as a function of C_t (Figure 4(a)). The errors vary slightly for all of the schemes except for MUSCL. For the convergence of the temporal integration, the MUSCL has to choose a smaller time step than the value prescribed by the CFL condition. But note this is only a test in linear case; in practical applications, coefficient C_t may be much smaller for convergence (Section 4.6).

To test the spatial convergence, we fix $C_t = 0.1$, and vary the number of mesh nodes N. The log–log plot of $\|E\|$ against Δx can be seen in Figure 4(c). We have two main observations. First, all of the schemes converge with an order between 1 and 2 and the DG scheme converges faster (Figure 4(c)). Second, as shown by Figure 4(d), the
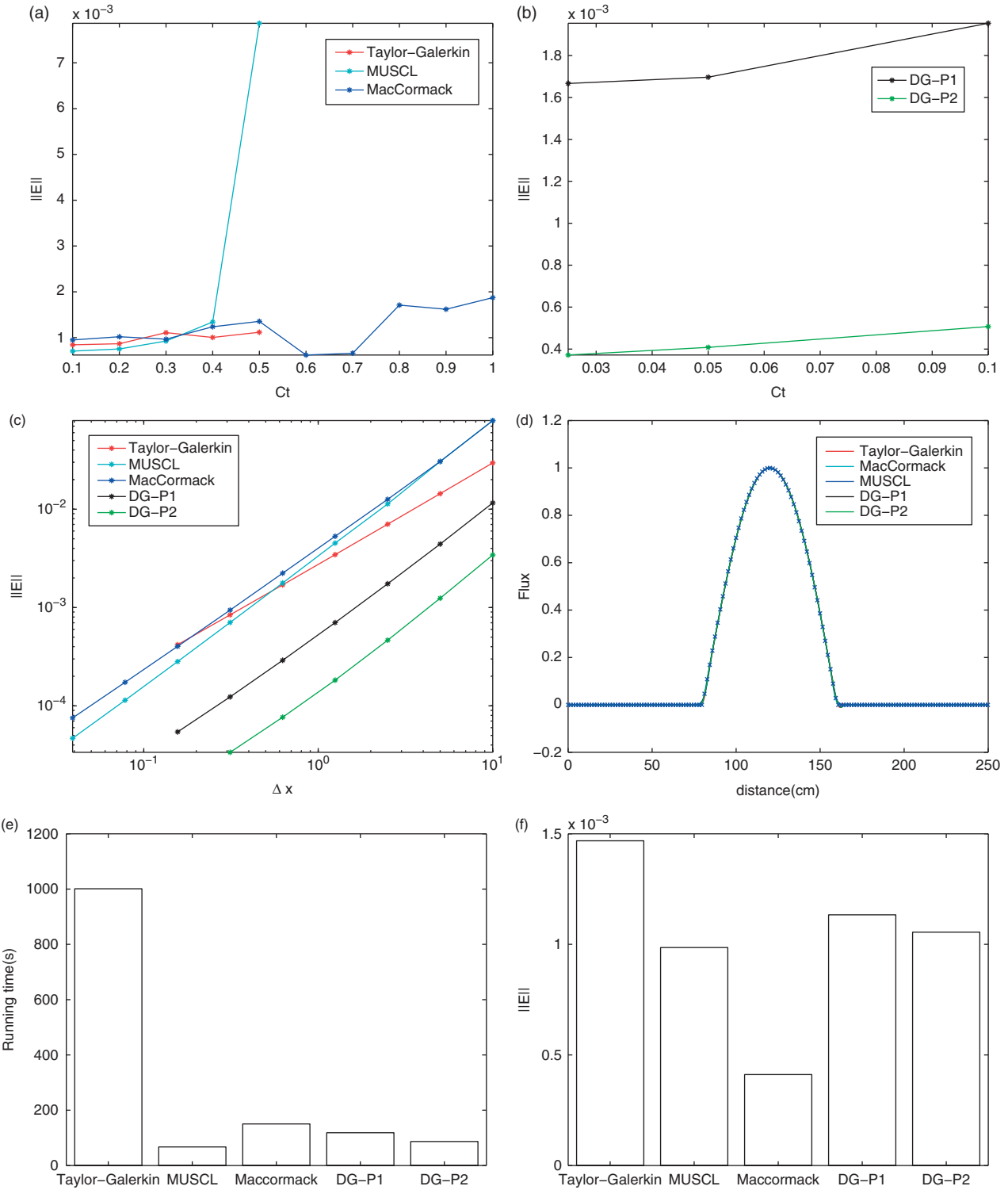
Figure 4.   Test on a uniform tube. Top left and right: with a fixed mesh ($N_{\mathrm{TG}} = N_{\mathrm{MUSCL}} = N_{\mathrm{FD}} = 800, N_{\mathrm{DG}\text{-}\mathcal{P}_1} = N_{\mathrm{DG}\text{-}\mathcal{P}_2} = 100$), errors as functions of coefficient C_t. Middle left: errors as functions of the sizes of elements (cells). Middle right: all the numerical solutions for the pulse wave at time 0.4 s are overlapped, the analytical solution is indicated by cross signs. Bottom left and right: running time and error of each scheme for the configuration shown in Table 1.

Table 1. Number of elements and coefficient of time step.

Scheme	N	C_t
Taylor–Gakerkin	800	0.5
MUSCL	800	0.3
MacCormack	1600	0.5
DG-$\mathcal{P}_1$	200	0.1
DG-$\mathcal{P}_2$	100	0.1

differences between the analytical solution and all of the numerical solutions are hardly discernible with a moderate number of mesh points ($N_{TG} = N_{FV} = N_{FD} = 800$, $N_{DG-\mathcal{P}_1} = N_{DG-\mathcal{P}_2} = 100$).

To compare the actual speed and accuracy of the four schemes, we set N and C_t (Table 1) such that the errors achieve the same order of magnitude (Figure 4(f)). Except the Taylor–Galerkin scheme, all the schemes have a similar accuracy with very close running time (Figure 4(e),(f)). At this point, the Taylor–Galerkin scheme shows the worst accuracy and needs to run the longest time. We note that large global matrices arise in the Taylor–Galerkin scheme while the operators in other schemes are local and have small size. That explains the relative poor performance of the Taylor–Galerkin scheme even though a larger time step is allowed by this scheme. We will see that in case of a network of real size, the largest number N is about 100 and the Taylor–Galerkin scheme shows a good balanced property between accuracy and speed (Section 4.6).

4.2 Attenuation due to viscosity of blood

We now consider the same linearized equation (34) with the small term due to skin friction ($C_f \neq 0$ and $C_v = 0$). The main dynamics of the system will be grossly the same traveling wave but attenuated by viscosity of blood. This behavior can be predicted by asymptotic analysis. We have a small non-dimensional parameter $\epsilon_f = T_c C_f / A_0$, which is the ratio of the characteristic time of pulse T_c to the characteristic time of attenuation A_0/C_f. In order to see how the waveform slowly evolves when it propagates to, say, right, we make a change of variables to $\tau = \epsilon_f t$ and $\xi = x - c_0 t$ (slow time, moving frame). The two differential operators ∂_t and ∂_x expand as

$$\frac{\partial}{\partial t} = \frac{\partial \tau}{\partial t}\frac{\partial}{\partial \tau} + \frac{\partial \xi}{\partial t}\frac{\partial}{\partial \xi} = \epsilon_f \frac{\partial}{\partial \tau} - c_0 \frac{\partial}{\partial \xi}$$
$$\frac{\partial}{\partial x} = \frac{\partial \xi}{\partial x}\frac{\partial}{\partial \xi} = \frac{\partial}{\partial \xi}.$$

The solution has the asymptotic expansion

$$\tilde{A} = \tilde{A}_0 + \epsilon_f \tilde{A}_1 + \cdots, \quad \tilde{Q} = \tilde{Q}_0 + \epsilon_f \tilde{Q}_1 + \cdots$$

Substituting these into the governing equations expressed in new variables and collecting the terms with the same

order of ϵ_f, we have

$$\left(-c_0 \frac{\partial \tilde{A}_0}{\partial \xi} + \frac{\partial \tilde{Q}_0}{\partial \xi}\right) + \epsilon_f \left(\frac{\partial \tilde{A}_0}{\partial \tau} - c_0 \frac{\partial \tilde{A}_1}{\partial \xi} + \frac{\partial \tilde{Q}_1}{\partial \xi}\right) + \cdots = 0,$$
$$\left(-c_0 \frac{\partial \tilde{Q}_0}{\partial \xi} + c_0^2 \frac{\partial \tilde{A}_0}{\partial \xi}\right) + \epsilon_f \left(\frac{\partial \tilde{Q}_0}{\partial \tau} - c_0 \frac{\partial \tilde{Q}_1}{\partial \xi} + c_0^2 \frac{\partial \tilde{A}_1}{\partial \xi} + \frac{\tilde{Q}_0}{T_c}\right)$$
$$+ \cdots = 0.$$

We take the first-order term in ϵ_f in the first equation and substitute it in the first-order term in ϵ_f in the second equation. Then we obtain

$$\left(\frac{\partial \tilde{Q}_0}{\partial \tau} + c_0 \frac{\partial \tilde{A}_0}{\partial \tau} + \frac{\tilde{Q}_0}{T_c}\right) = 0.$$

From the terms of the zeroth order in ϵ_f, which involve derivative in ξ only, the solution must have the form $\tilde{Q}_0 = c_0 \tilde{A}_0(\tau, \xi) + \delta(\tau)$. Substituting it into the previous equation generates terms $\partial \delta/\partial \tau$ and $\delta(\tau)$. These are secular terms and thus can be set null. So we have $c_0 \tilde{A}_0 = \tilde{Q}_0$ and $\partial \tilde{Q}_0/\partial \tau = -(1/2T_c)\tilde{Q}_0$, or

$$\tilde{Q}_0 = \tilde{Q}_0(0, \xi)e^{-\tau/(2T_c)} = \tilde{Q}_0(0, x - c_0 t)e^{-\epsilon_f t/(2T_c)}.$$

For more on asymptotic analysis of blood flow in large blood vessels, we refer to Yomosa (1987).

In Figure 5, we plot the snapshots of the waveform at time 0.2, 0.4, 0.6, and 0.8 s. In the computation, the inflow is a half sinusoidal flux as described in the previous subsection and the outflow is non-reflecting. The skin friction coefficient C_f is $40\nu\pi$, and the parameter $2A_0 c_0/C_f$ is about 2000 cm. The damping rate of the amplitude of the waveform agrees very well with the analytical prediction, $\exp(-(C_f x/2A_0 c_0))$, which is
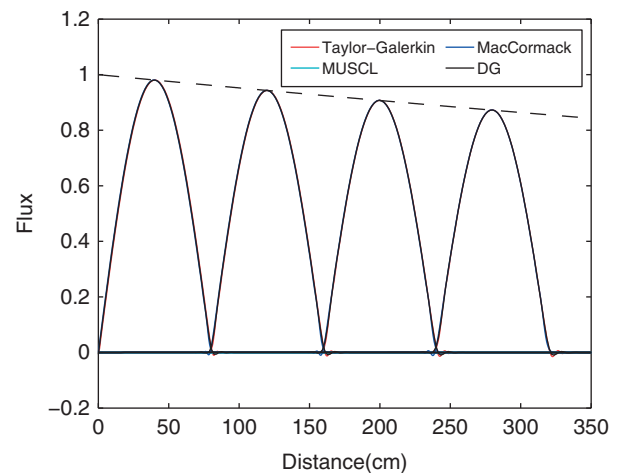

Figure 5. Attenuation due to skin friction. The snapshots are at time 0.2, 0.4, 0.6, and 0.8 s. The dashed line is $\exp(-C_f x/2A_0 c_0)$ with $2A_0 c_0/C_f \simeq 2000$ cm. The flux is normalized with respect to Q_c.

indicated by the dashed line. Also note that the errors of different schemes are not the same. The MUSCL causes the peak of the wave to slightly flatten, while all of the other schemes are dispersive: we have small oscillations at the foot of the signal.

4.3   Diffusion due to the viscosity of the arterial wall

This time we consider the linearized equations (34) with the Kelvin–Voigt effect but no viscous fluid effect ($C_f = 0$ and $C_v \neq 0$). The small parameter is now $\epsilon_v = C_v/(c_0^2 T_c)$. If we apply the same technique as described in the previous subsection, we can readily obtain the diffusive behavior of the pulse wave in the moving frame:

$$\frac{\partial \tilde{Q}_0}{\partial \tau} = \frac{c_0^2 T_c}{2} \frac{\partial^2 \tilde{Q}_0}{\partial^2 \xi}. \tag{35}$$

The solution of this equation can be given by the convolution

$$\tilde{Q}_0(\tau, \xi) = \int_{-\infty}^{+\infty} \tilde{Q}_0(0, \xi) G(\tau, \xi - \zeta) d\zeta,$$

where G is the fundamental solution of Equation (35)

$$G(\tau, \xi) = \frac{1}{\sqrt{2\pi\tau c_0^2 T_c}} e^{-\xi^2/(2\pi c_0^2 T_c)}$$

and $\tilde{Q}_0(0, \xi)$ is the initial state. In the test vessel, the parameters are kept the same as in the case of attenuation. Coefficient C_v is $0.6275\,\mathrm{m}^2/\mathrm{s}$ and $\epsilon_v \simeq 0.1$. This corresponds to $\phi = 5000\,\mathrm{Pa\,s}$, which is in the range of observed values on animals (Armentano et al. 1995). To facilitate the calculation of the analytical solution, non-reflecting BCs are imposed at the two ends of the vessel and the IC is a half sinusoidal waveform for Q (dashed line in Figure 6) and a constant value for A_0. It is clear that half of the initial wave propagates to the right and at the same time the waveform is spread out due to the diffusive effect. The analytical solution at time 0.4 s (indicated by cross signs) agrees well with the corresponding numerical solutions.

Another point worthy noticing is the operator splitting errors. In the DG scheme, no operator splitting error is induced. All of the other numerical schemes adopt the operator splitting method. They produce very accurate solutions as well as DG. Thus it verifies the *a priori* judgment that Godunov splitting is sufficient.

4.4   Shock-like phenomena due to the nonlinearity

We now consider the full nonlinear system, but without any source terms ($C_f = 0$ and $C_v = 0$). The small
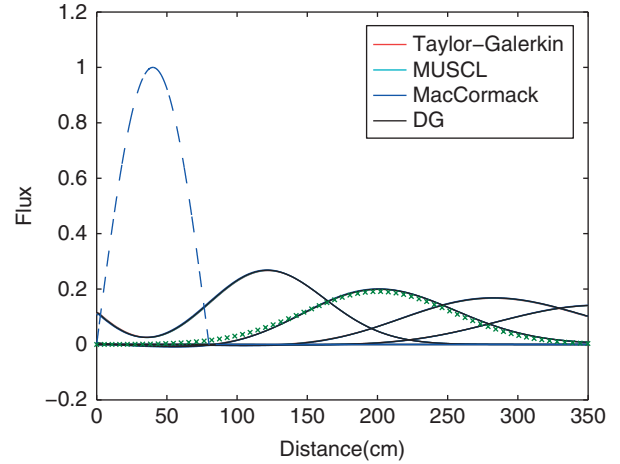

Figure 6.   Diffusion due to viscosity of the wall. The dashed line is the IC. One half of the original waveform propagates to right. The snapshots are at time 0.2, 0.4, 0.6, and 0.8 s. The analytical prediction from the convolution at time 0.4 s is indicated by cross signs. The difference between the different numerical solutions is not discernible. The flux is normalized with respect to Q_c.

parameter is now $\epsilon_2 = Q_c/(c_0 A_0)$. If we apply the same technique as described in the previous subsection, we can readily obtain an equation for the nonlinear behavior of the pulse wave in the moving frame (inviscid Burgers' equation):

$$\frac{\partial \tilde{Q}_0}{\partial \tau} = \frac{1}{2A_0} \tilde{Q}_0 \frac{\partial \tilde{Q}_0}{\partial \xi}.$$

One important consequence of the nonlinear hyperbolic system is that shocks may arise even if the IC is very smooth. In normal physiological conditions, shocks are not observed in arterial systems. But in the venous system, shock-like phenomena may occur on muscular veins during walking and running. The intramuscular pressure (equivalent to P_{ext} in our model) can rise to $20 - 40\,\mathrm{kPa}$ in a few milliseconds (Ballard et al. 1998). In such a situation, experiments and numerical simulations (Marchandise and Flaud 2010; Flaud et al. 2012) have shown this critical behavior. For some large mammals, for instance giraffes, even in static postures, the gravity-driven flow in a long inclined vein may develop into shock-like waves, like the roll waves in a shallow water channel (Brook et al. 1999; Brook and Pedley 2002). For another example, the traumatic rupture of the aorta is responsible for a significant percentage of traffic death and the rupture may be well accounted for by the shock-like transition resulted from the blunt impact to the thorax (Kivity and Collins 1974). For possible applications in these situations, we test all the schemes with a shock-like wave.

To generate a shock, we impose a step jump signal of flux at the inlet. For a vessel of 1 m, the number of elements for Taylor–Galerkin, MacCormack, and
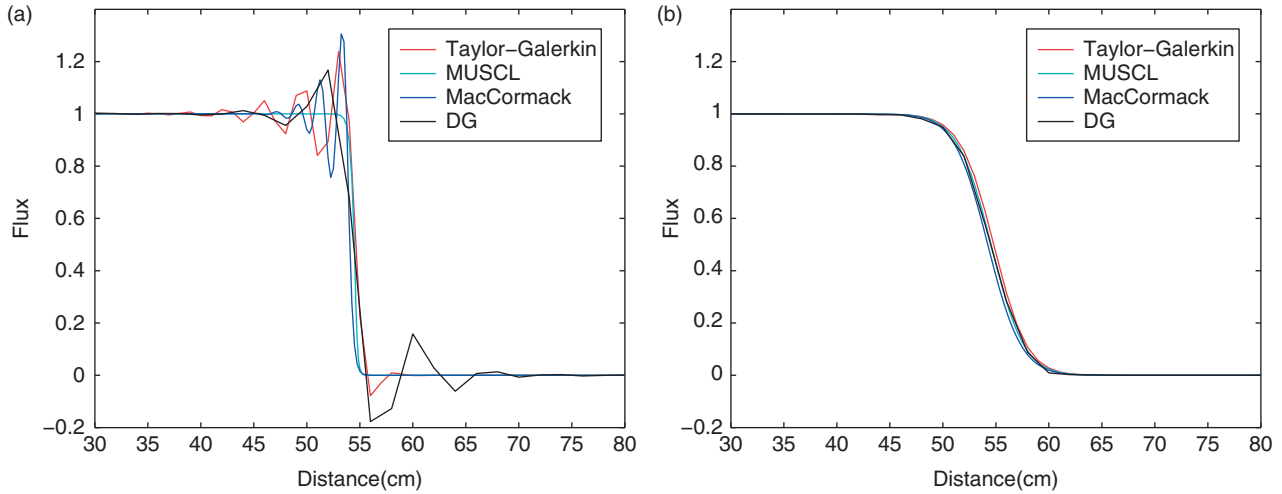
Figure 7. A shock in the system. A step jump signal of flux is imposed at the inlet and a snapshot is shown. (a) Shows that the MUSCL with a flux limiter captures the shock without non-physical oscillations, whereas the other numerical schemes cause spurious oscillations. (b) Shows that all the schemes give almost the same result for a system with a moderate physical diffusive term.

MUSCL schemes are 100, 200, and 800, respectively. The DG scheme uses 25 elements and the order of polynomial is 2. Figure 7 shows that the MUSCL with a flux limiter captures the shock without non-physical oscillations, whereas the other numerical schemes cause spurious oscillations. This verifies the total-variation-diminishing property of the MUSCL. But the MUSCL is very diffusive at the shock, thus a very fine mesh is required. For the DG scheme, limiters may be introduced as well to eliminate the oscillations (Hesthaven and Warburton 2008). This remedy will be necessary for DG to be applicable on problems with shocks. On Figure 7(b) we plot a case with some viscosity of the wall. The added moderate physical diffusive term smoothens the wave and all the schemes give almost the same result.

4.5 Reflection and transmission at a branching point

Up to now, we focused on the various behaviors of wave within a single vessel: propagation, attenuation, diffusion, etc. Now, we look at the boundaries of each artery. Indeed, pressure waves are reflected and transmitted at the conjunction points of a network. For a linearized system, given the impedance $Z = \rho c_0 / A_0$, the reflection and transmission coefficients at a branching point can be calculated by the formula

$$\mathcal{R} = \frac{Z_p^{-1} - \left(Z_{d_1}^{-1} + Z_{d_2}^{-1}\right)}{Z_p^{-1} + \left(Z_{d_1}^{-1} + Z_{d_2}^{-1}\right)},$$

$$\mathcal{T} = \frac{2Z_p^{-1}}{Z_p^{-1} + \left(Z_{d_1}^{-1} + Z_{d_2}^{-1}\right)},$$

(36)

where Z_p and Z_d are the characteristic impedance of the parent and daughter vessels (Pedley 1980; Fung 1997). In Figure 8, for sake of illustration, the configuration of the branching and the time profiles of pressure at two locations are shown. The amplitude is normalized with respect to $Q_c = 1 \times 10^{-6} \, \text{m}^3/\text{s} = 1 \, \text{ml/s}$. For the parent vessel, $\beta = 2.3633 \times 10^6 \, \text{Pa/m}$ and $A_0 = 4 \, \text{cm}^2$, and for each of the daughter vessels, $\beta = 6.3021 \times 10^6 \, \text{Pa/m}$ and $A_0 = 1.5 \, \text{cm}^2$. The BCs at the outlets of the daughter vessels are non-reflecting. Thus the reflected pulse wave is generated at the conjunction point. According to the formula (36), $\mathcal{R} = 0.2603$ and $\mathcal{T} = 1.2603$. The pressure profiles at points A and B agree very well with the analytical predictions. All of the numerical schemes are compatible with this treatment of
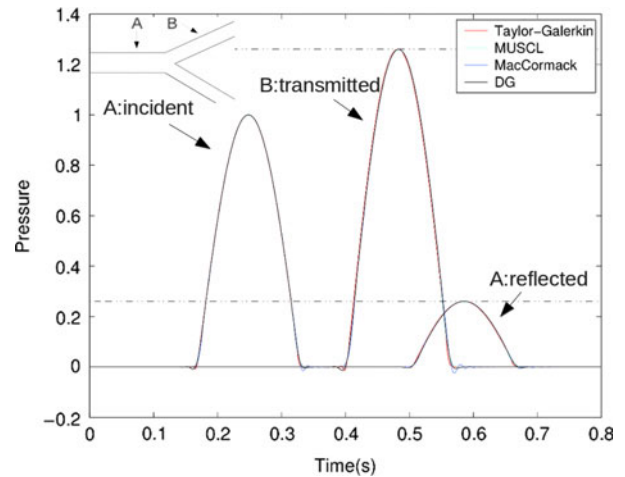

Figure 8. Reflection and transmission of pressure wave at a branching point. The time profiles of pressure at points A and B are plotted. The analytical reflection and transmission coefficients are 0.2603 and 1.2603 (indicated by the dashed line).

Table 2.   Arterial network.

ID	Name	L (cm)	A_0 (cm^2)	β (10^6 Pa/cm)	C_v (10^4 cm^2/s)	R_t
1	Ascending aorta	4.0	6.789	0.023	0.352	–
2	Aortic arch I	2.0	5.011	0.024	0.317	–
3	Brachiocephalic	3.4	1.535	0.049	0.363	–
4	R. subclavian I	3.4	0.919	0.069	0.393	–
5	R. carotid	17.7	0.703	0.085	0.423	–
6	R. vertebral	14.8	0.181	0.470	0.595	0.906
7	R. subclavian II	42.2	0.833	0.076	0.413	–
8	R. radius	23.5	0.423	0.192	0.372	0.82
9	R. ulnar I	6.7	0.648	0.134	0.322	–
10	R. interosseous	7.9	0.118	0.895	0.458	0.956
11	R. ulnar II	17.1	0.589	0.148	0.337	0.893
12	R. int. carotid	17.6	0.458	0.186	0.374	0.784
13	R. ext. carotid	17.7	0.458	0.173	0.349	0.79
14	Aortic arch II	3.9	4.486	0.024	0.306	–
15	L. carotid	20.8	0.536	0.111	0.484	–
16	L. int. carotid	17.6	0.350	0.243	0.428	0.784
17	L. ext. carotid	17.7	0.350	0.227	0.399	0.791
18	Thoracic aorta I	5.2	3.941	0.026	0.312	–
19	L. subclavian I	3.4	0.706	0.088	0.442	–
20	L. vertebral	14.8	0.129	0.657	0.704	0.906
21	L. subclavian II	42.2	0.650	0.097	0.467	–
22	L. radius	23.5	0.330	0.247	0.421	0.821
23	L. ulnar I	6.7	0.505	0.172	0.364	–
24	L. interosseous	7.9	0.093	1.139	0.517	0.956
25	L. ulnar II	17.1	0.461	0.189	0.381	0.893
26	intercoastals	8.0	0.316	0.147	0.491	0.627
27	Thoracic aorta II	10.4	3.604	0.026	0.296	–
28	Abdominal aorta I	5.3	2.659	0.032	0.311	–
29	Celiac I	2.0	1.086	0.056	0.346	–
30	Celiac II	1.0	0.126	0.481	1.016	–
31	Hepatic	6.6	0.659	0.070	0.340	0.925
32	Gastric	7.1	0.442	0.096	0.381	0.921
33	Splenic	6.3	0.468	0.109	0.444	0.93
34	Sup. mensenteric	5.9	0.782	0.083	0.439	0.934
35	Abdominal aorta II	1.0	2.233	0.034	0.301	–
36	L. renal	3.2	0.385	0.130	0.481	0.861
37	Abdominal aorta III	1.0	1.981	0.038	0.320	–
38	R. renal	3.2	0.385	0.130	0.481	0.861
39	Abdominal aorta IV	10.6	1.389	0.051	0.358	–
40	Inf. mesenteric	5.0	0.118	0.344	0.704	0.918
41	Abdominal aorta V	1.0	1.251	0.049	0.327	–
42	R. com. iliac	5.9	0.694	0.082	0.405	–
43	L. com. iliac	5.8	0.694	0.082	0.405	–
44	L. ext. iliac	14.4	0.730	0.137	0.349	–
45	L. int. iliac	5.0	0.285	0.531	0.422	0.925
46	L. femoral	44.3	0.409	0.231	0.440	–
47	L. deep femoral	12.6	0.398	0.223	0.419	0.885
48	L. post. tibial	32.1	0.444	0.383	0.380	0.724
49	L. ant. tibial	34.3	0.123	1.197	0.625	0.716
50	L. ext. iliac	14.5	0.730	0.137	0.349	–
51	R. int. iliac	5.0	0.285	0.531	0.422	0.925
52	R. femoral	44.4	0.409	0.231	0.440	–
53	R. deep femoral	12.7	0.398	0.223	0.419	0.888
54	R. post. tibial	32.2	0.442	0.385	0.381	0.724
55	R. ant. tibial	34.4	0.122	1.210	0.628	0.716

Source: Data adapted from Sherwin et al. (2003) and Armentano et al. (1995).

conjunction point. Note that in a healthy arterial system, the related arteries of most conjunctions are well matched such that there are essentially no reflections ($\mathcal{R} = 0$) at the conjunctions (Papageorgiou et al. 1990; Wang and Parker 2004). The purpose of the proposed configuration is just to test the numerical schemes.
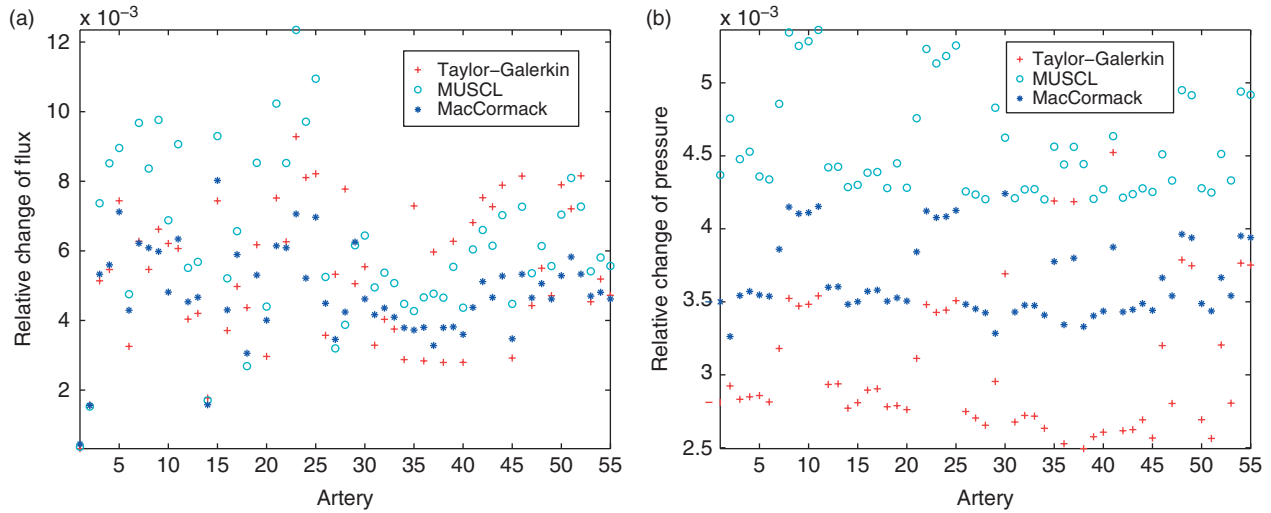
Figure 9. Relative changes of the solutions when the mesh is doubled from $2N_{\text{base}}$ to $4N_{\text{base}}$. The left figure shows that the relative changes of all the fluxes are less than 1.3%. The right figure shows that the relative changes of all the pressures are less than 0.6%.

4.6 Application on a full systematic arterial network

As already mentioned in the introduction, a relatively realistic description of an arterial system has been done in 1D simulations, with different numerical solvers by different teams. For example, in Mynard and Nithiarasu (2008) and Sherwin et al. (2003), the Galerkin approach is used. In these papers, wall viscosity is not included. Note that Reymond et al. (2009) gives a survey of the literature on the details of the model, and adopted a viscoelastic model of the wall. But, in all of those papers, usually only one numerical scheme is adopted and cross comparisons among them are not available. In this subsection, we compute a network of 55 arteries with the viscoelastic model presented above and make a cross comparison among the numerical schemes. To this end, the topology and properties value of the arterial network are adapted from Sherwin et al. (2003). But the viscosity coefficient of the Kelvin–Voigt model on the human body is not given in this paper. In Armentano et al. (1995), the viscosity of the aortic wall of dogs was modeled by a Kelvin–Voigt model and it shows that the value of ϕ is in the range of $3.8 \pm 1.3 \times 10^3$ to $7.8 \pm 1.1 \times 10^3$ Pa·s. Hence, we assume $\phi = 5 \times 10^3$ Pa·s to calculate coefficient C_v. The final parameters of the network we used are shown in Table 2. We note that there may be differences between arteries in humans and dogs and the arteries in different locations may cause a considerable variation. Nevertheless, the inclusion of viscosity term makes it possible to test the numerical schemes in a more realistic condition.

The peak value of the input flux Q_c is 500 ml/s. This value is very close to the peak flow rate at the root of the aortic artery (Reymond et al. 2009). We choose $\min_{i=1}^{i=55}(L^i/c_0^i)$ as a reference length, with L^i being the vessel length and c_0^i the linearized wave speed of the i-th

artery. For a coarsest possible mesh, the number of elements (cells) of the i-th artery is $N_{\text{base}}^i = \lfloor \frac{L^i/c_0^i}{\min_{i=1}^{i=55}(L^i/c_0^i)} \rfloor$, where $\lfloor \cdot \rfloor$ is the floor function. We computed the relative change of solutions when the number of elements (cells) is doubled. Figure 9 shows the relative change of the solutions when the number of elements (cells) is changed from $2N_{\text{base}}$ to $4N_{\text{base}}$. The relative change of a quantity (e.g. flux Q) with two meshes N_1 and N_2 is defined as $\|\mathbf{Q}_{N_1} - \mathbf{Q}_{N_2}\|_{\text{rms}}/(Q_{\text{max}} - Q_{\text{min}})$, where $\|\cdot\|_{\text{rms}}$ is the root-mean-square error as before, Q_{max} and Q_{min} are the maximum and minimum values within one heartbeat. Figure 9 shows that the changes of flux and pressure are less than 1.5% for all of the schemes except DG. Thus we plotted in Figure 10 the results computed with mesh $2N_{\text{base}}$. The DG scheme is not tested in this manner because it is already converged: results in Figure 10 show that there is no discernible difference between the DG solutions with the others even with the coarsest possible mesh. In this computation, the order of polynomial of DG is 1, thus the total number of free degrees is $2N_{\text{base}}$, which is equal to those of the other schemes. Time step is prescribed by $\Delta t = C_t \min_{i=1}^{i=55}(L^i/N^i c_0^i)$. Coefficient C_t and the corresponding real time steps in the computation are shown in Table 3.

In Figure 10 we plot the history profiles of flux and pressure at the middle of four representative arteries. All of the numerical solutions agree very well. The main features of the pressure and flux profiles reported in the literature (Sherwin et al. 2003; Reymond et al. 2009) are observed. The peak value of pressure waveform increases as we travel down the system. We can also see the dicrotic notch at artery 1. At artery 37, a reverse flow is observed (Figure 10(f)), which agrees with clinical measurement (Reymond et al. 2009).
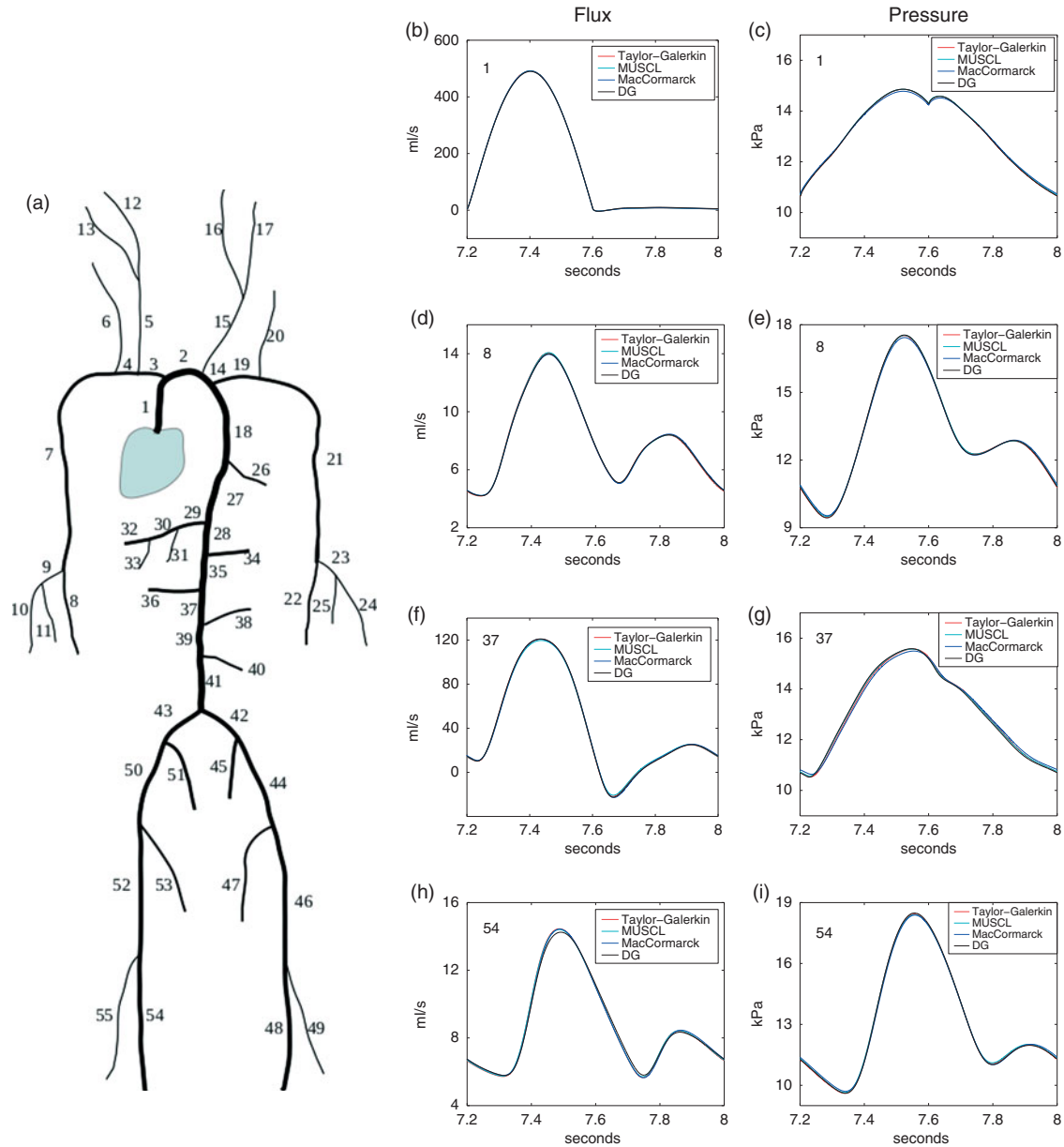
Figure 10.   The history profiles of flux and pressure at four locations. Ten heartbeats are computed to secure that steady state is achieved, but only the tenth heartbeat is plotted. The differences between the four numerical schemes are very small. See Table 2 for time steps and running time of each scheme.

Both *in vivo* (Holenstein et al. 1980; Reymond et al. 2009) and *in vitro* (Alastruey et al. 2011) studies show that the models with viscoelasticity predict the pulse waves better. This effect is most pronounced at the peripheral sites

Table 3.   Time steps and running time for one heartbeat using one processor on a standard Linux workstation with MATLAB.

Scheme	C_t	Δt (10^{-6} s)	Running time (min)
Taylor–Gakerkin	0.4	222	22.0
MUSCL	0.25	139	31.9
MacCormack	0.1	55.5	91.2
Local DG	0.006	6.66	576

(Segers et al. 1997; Alastruey et al. 2011). The predictions by the elastic and viscoelastic models are compared at two locations, see Figure 11. We can clearly see the smoothing effect on the pulse curves at both sites. The biggest relative difference is observed on the flow rate curve at the peripheral site (Figure 11(c)). This study confirms again the necessity to consider the viscoelasticity in the 1D model.

5.   Conclusions

In this paper, we incorporated a Kelvin–Voigt viscoelastic constitutive relation of arterial wall with a 1D blood flow
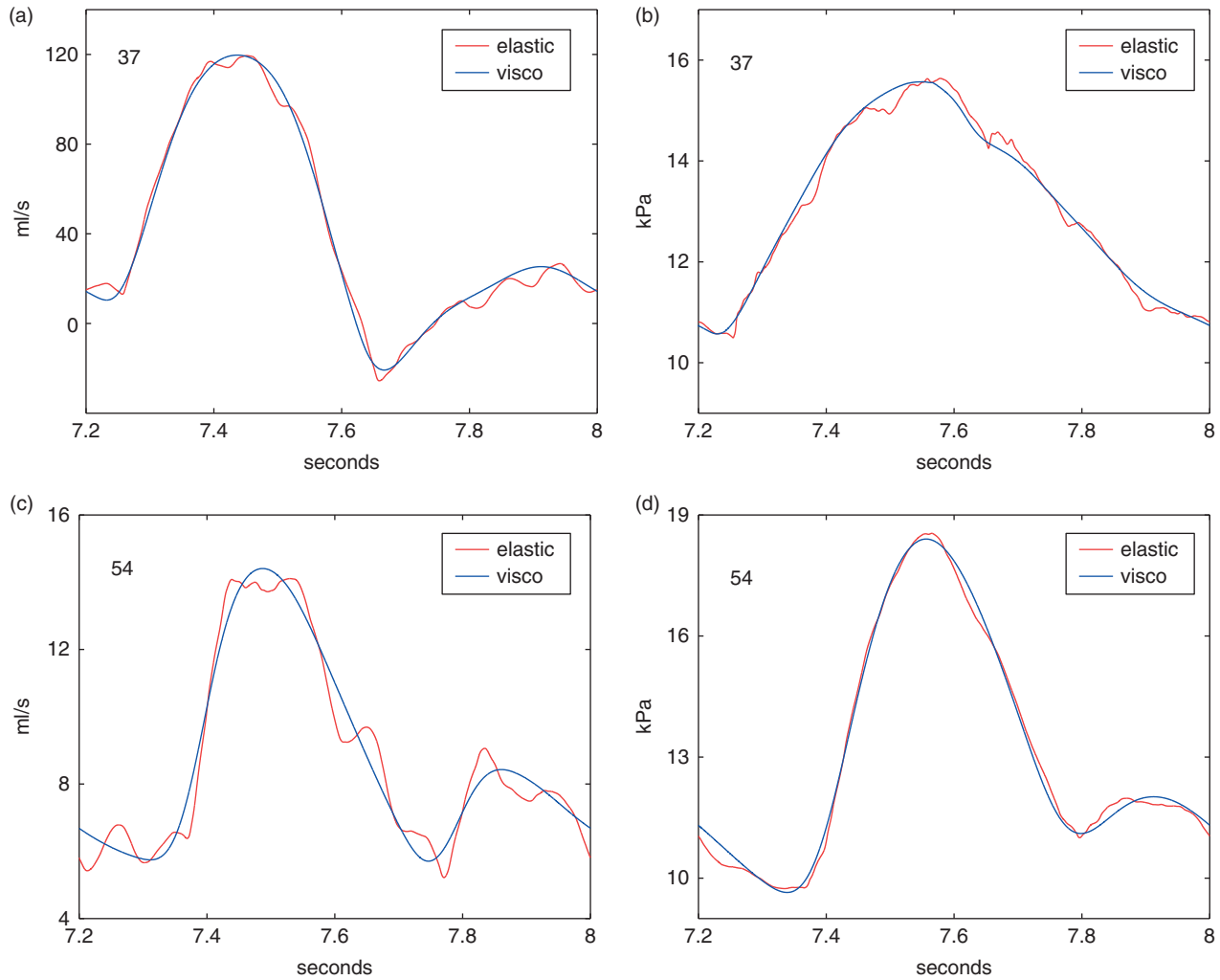
Figure 11. The comparison between elastic and viscoelastic models (MUSCL). Viscoelasticity damps the oscillations of high frequency.

model. This led to a hyperbolic–parabolic system which was then solved by four numerical schemes: MacCormack, Taylor–Galerkin, MUSCL, and local DG. The implementations were verified with analytical, semi-analytical, or clinical observations in many cases. At first, a single uniform tube was considered. Under the assumption of small nonlinearities, we obtained asymptotic solutions of the linearized system with different source terms. The propagation, attenuation, and diffusion of the waveform were illustrated by both the numerical and analytical solutions. Moreover, in case of a larger nonlinearity, the shock-capturing property of each scheme was tested. After the test on a single vessel, a simple bifurcation was computed to check the numerical coupling of different arteries. Finally, we computed a relatively realistic network with 55 arteries. The check of the numerical solutions in all cases was very favorable for all of the schemes. We can compare the schemes in four aspects: accuracy, shock-capturing property, computational speed, and implementation complexity.

1. MacCormack and Taylor–Galerkin schemes generate small oscillations. MUSCL has slight arbitrary steepening effect. Both diffusion and dispersion errors are very small for DG. Nevertheless all of the schemes converge with a moderate fine mesh and precisely capture the various phenomena of this hyperbolicity-dominated hyperbolic–parabolic system.
2. MacCormack, Taylor–Galerkin and DG schemes generate spurious oscillations when the solution is near a shock. Numerical flux limiters are possible to filter out the oscillations. That will further complicate the schemes and both the theory and technique are still under research (Marchandise and Flaud 2010; Kuzmin 2012). On the other hand, there are very mature techniques to impose a slope limiter in the FV scheme. Shock-capturing property is unique for MUSCL among the four schemes presented in this paper. But it is very diffusive at a shock, thus a very fine mesh is necessary when a shock may appear.

3. For a network of human size, the speed of computation can be ordered from fast to slow as follows: Taylor–Galerkin, MUSCL, MacCormack, and local DG. The temporal integration in the Taylor–Galerkin scheme is more efficient than the A–B two-step method. Thus it allows a larger time step with a comparable accuracy. But if the number of elements for one artery is too large (larger than 500), the Taylor–Galerkin scheme becomes slower because the sizes of the global matrices increase quadratically and thus the storing and inverting of matrices become very expensive. The DG scheme prevents the application of the Crank–Nicolson method on the diffusive term. An explicit method called local DG scheme was adopted in this paper. Even with a moderate diffusion coefficient (within the range observed in physiological condition), a very small time step is necessary for stability. To compute one heartbeat, the local DG takes about 9 h while all other schemes take only 20–90 min (using one processor on a standard Linux workstation with MATLAB).

4. From easiest to hardest, the implementation of the schemes can be ordered as follows: MacCormack, MUSCL, Taylor–Galerkin, and local DG.

As a final conclusion from the point of view of practical application, we recommend MacCormack in case of small nonlinearities as it is very simple and robust. MUSCL will be a very good option if there may be shock-like phenomena in the system. Taylor–Galerkin has quite balanced properties between speed and accuracy if no shock-like phenomena may be present in the system. Local DG is suitable for systems with very small physical diffusive terms since both the numerical diffusion and dispersion are very small in this scheme.

Notes

1. Email: fullana@lmm.jussieu.fr
2. Email: pierre-yves.lagree@upmc.fr

References

Alastruey J, Khir AW, Matthys KS, Segers P, Sherwin SJ, Verdonck PR, Parker KH, Peiró J. 2011. Pulse wave propagation in a model human arterial network: assessment of 1-D visco-elastic simulations against *in vitro* measurements. J Biomech. 44:2250–2258.

Armentano RL, Barra JG, Levenson J, Simon A, Pichel RH. 1995. Arterial wall mechanics in conscious dogs: assessment of viscous, inertial, and elastic moduli to characterize aortic wall behavior. Circ Res. 76(3):468–478.

Ballard RE, Watenpaugh DE, Breit GA, Murthy G, Holley DC, Hargens AR. 1998. Leg intramuscular pressures during locomotion in humans. J Appl Physiol. 84(6):1976–1981.

Barnard ACL, Hunt WA, Timlake WP, Varley E. 1966. A theory of fluid flow in compliant tubes. Biophys J. 6(6):717–724.

Bertoglio C, Moireau Ph, Gerbeau J-F. 2012. Sequential parameter estimation for fluid–structure problems: application to hemodynamics. Int J Numer Method Biomed Eng. 28:434–455.

Blacher J, Asmar R, Djane S, London GM, Safar ME. 1999. Aortic pulse wave velocity as a marker of cardiovascular risk in hypertensive patients. Hypertension. 33(5):1111–1117.

Bouchut F. 2004. Nonlinear stability of finite volume methods for hyperbolic conservation laws and well-balanced schemes for sources. Birkhäuser. Basel: Springer.

Brook BS, Falle SAEG, Pedley TJ. 1999. Numerical solutions for unsteady gravity-driven flows in collapsible tubes: evolution and roll-wave instability of a steady state. J Fluid Mech. 396(1):223–256.

Brook BS, Pedley TJ. 2002. A model for time-dependent flow in (giraffe jugular) veins: uniform tube properties. J Biomech. 35(1):95–107.

Cavallini N, Caleffi V, Coscia V. 2008. Finite volume and weno scheme in one-dimensional vascular system modelling. Comput Math Appl. 56(9):2382–2397.

Crosetto P, Reymond Ph, Deparis S, Kontaxakis D, Stergiopulos N, Quarteroni A. 2011. Fluid–structure interaction simulation of aortic blood flow. Comput Fluids. 43(1):46–57.

Delestre O, Lagrée P-Y. 2012. A 'well balanced' finite volume scheme for blood flow simulation. Int J Numer Methods Fluids., doi: 10.1002/fld.3736.

DeVault K, Gremaud PA, Novak V, Olufsen MS, Vernieres G, Zhao P. 2008. Blood flow in the circle of Willis: modeling and calibration. Multiscale Model Simul. 7(2):888–909.

Di Martino ES, Guadagni G, Fumero A, Ballerini G, Spirito R, Biglioli P, Redaelli A. 2001. Fluid–structure interaction within realistic three-dimensional models of the aneurysmatic aorta as a guidance to assess the risk of rupture of the aneurysm. Med Eng Phys. 23(9):647–655.

Elad D, Katz D, Kimmel E, Einav S. 1991. Numerical schemes for unsteady fluid flow through collapsible tubes. J Biomed Eng. 13(1):10–18.

Flaud P, Guesdon P, Fullana J-M. 2012. Experiments of draining and filling processes in a collapsible tube at high external pressure. Eur Phys J Appl Phys. 57(3):223–256.

Formaggia L, Gerbeau J-F, Nobile F, Quarteroni A. 2001. On the coupling of 3D and 1D Navier–Stokes equations for flow problems in compliant vessels. Comput Methods Appl Mech Eng. 191(6):561–582.

Formaggia L, Lamponi D, Quarteroni A. 2003. One-dimensional models for blood flow in arteries. J Eng Math. 47:251–276.

Formaggia L, Quarteroni A, Veneziani A. 2009. Cardiovascular mathematics: modeling and simulation of the circulatory system. Vol. 1. Milan: Springer.

Fullana J-M, Zaleski S. 2009. A branched one-dimensional model of vessel networks. J Fluid Mech. 621(1):183–204.

Fung Y. 1997. Biomechanics: circulation. New York: Springer Verlag.

Gerbeau J-F, Vidrascu M, Frey P. 2005. Fluid–structure interaction in blood flows on geometries based on medical imaging. Comput Struct. 83(2):155–165.

Hesthaven JS, Warburton T. 2008. Nodal discontinuous Galerkin methods: algorithms, analysis, and applications. Vol. 54. New York: Springer-Verlag.

Holenstein R, Niederer P, Anliker M. 1980. A viscoelastic model for use in predicting arterial pulse waves. J Biomech Eng. 102(4):318–325.

Hughes TJ, Lubliner J. 1973. On the one-dimensional theory of blood flow in the larger vessels. Math Biosci. 18(1):161–170.

Kivity Y, Collins R. 1974. Nonlinear wave propagation in viscoelastic tubes: application to aortic rupture. J Biomech. 7(1):67–76.

Kuzmin D. 2012. Slope limiting for discontinuous Galerkin approximations with a possibly non-orthogonal Taylor basis. Int J Numer Methods Fluids. 71:1178–1190.

Lagrée P-Y. 2000. An inverse technique to deduce the elasticity of a large artery. EPJ Appl Phys. 9(2):153–164.

Lagrée P-Y, Rossi M. 1996. Etude de l'écoulement du sang dans les artères: effets nonlinéaires et dissipatifs [Blood flow in arteries: nonlinear and dissipative effects]. CR Acad Sci II B. 322(5):401–408.

LeVeque RJ. 2002. Finite volume methods for hyperbolic problems. Vol. 31. Cambridge: Cambridge University Press.

Li Z, Kleinstreuer C. 2005. Blood flow and structure interactions in a stented abdominal aortic aneurysm model. Med Eng Phys. 27(5):369–382.

Lighthill J. 2001. Waves in fluids. Cambridge: Cambridge University Press.

MacCormack RW. 2003. The effect of viscosity in hypervelocity impact cratering. J Spacecraft Rockets. 40(5):757–763.

Malossi ACI, Blanco PJ, Deparis S. 2012. A two-level time step technique for the partitioned solution of one-dimensional arterial networks. Comput Methods Appl Mech Eng. 237:212–226.

Mancia G, De Backer G, Dominiczak A, Cifkova R, Fagard R, Germano G, Grassi G, Heagerty AM, Kjeldsen SE, Laurent S, et al. 2007. 2007 Guidelines for the management of arterial hypertension the task force for the management of arterial hypertension of the European Society of Hypertension (ESH) and of the European Society of Cardiology (ESC). Eur Heart J. 28(12):1462–1536.

Marchandise E, Flaud P. 2010. Accurate modelling of unsteady flows in collapsible tubes. Comput Methods Biomech Biomed Eng. 13(2):279–290.

Marchandise E, Willemet M, Lacroix V. 2009. A numerical hemodynamic tool for predictive vascular surgery. Med Eng Phys. 31(1):131–144.

Matthys KS, Alastruey J, Peiró J, Khir AW, Segers P, Verdonck PR, Parker KH, Sherwin SJ. 2007. Pulse wave propagation in a model human arterial network: assessment of 1-D numerical simulations against *in vitro* measurements. J Biomech. 40(15):3476–3486.

Mynard JP, Nithiarasu P. 2008. A 1D arterial blood flow model incorporating ventricular pressure, aortic valve and regional coronary flow using the locally conservative Galerkin (LCG) method. Commun Numer Methods Eng. 24(5):367–417.

Nicoud F, Vernhet H, Dauzat M. 2005. A numerical assessment of wall shear stress changes after endovascular stenting. J Biomech. 38(10):2019–2027.

Nobile F. 2009. Coupling strategies for the numerical simulation of blood flow in deformable arteries by 3D and 1D models. Math Comput Model. 49(11):2152–2160.

Olufsen MS, Peskin C, Kim WY, Pedersen EM, Nadim A, Larsen J. 2000. Numerical simulation and experimental validation of blood flow in arteries with structured-tree outflow conditions. Ann Biomed Eng. 28(11):1281–1299.

Papageorgiou GL, Jones BN, Redding VJ, Hudson N. 1990. The area ratio of normal arterial junctions and its implications in pulse wave reflections. Cardiovasc Res. 24(6):478–484.

Pedley T. 1980. The fluid mechanics of large blood vessels. Cambridge: Cambridge University Press.

Perktold K, Rappitsch G. 1995. Computer simulation of local blood flow and vessel mechanics in a compliant carotid artery bifurcation model. J Biomech. 28(7):845–856.

Pullan AJ, Smith NP, Hunter PJ. 2002. An anatomically based model of transient coronary blood flow in the heart. SIAM J Appl Math. 62(3):990–1018.

Raghu R, Taylor CA. 2011. Verification of a one-dimensional finite element method for modeling blood flow in the cardiovascular system incorporating a viscoelastic wall model. Finite Elem Anal Des. 47(6):586–592.

Raghu R, Vignon-Clementel IE, Figueroa CA, Taylor CA. 2011. Comparative study of viscoelastic arterial wall models in nonlinear one-dimensional finite element simulations of blood flow. J Biomech Eng. 133(8):081003.

Reymond P, Bohraus Y, Perren F, Lazeyras F, Stergiopulos N. 2011. Validation of a patient-specific one-dimensional model of the systemic arterial tree. Am J Physiol Heart Circ Physiol. 301(3):H1173–H1182.

Reymond P, Merenda F, Perren F, Rüfenacht D, Stergiopulos N. 2009. Validation of a one-dimensional model of the systemic arterial tree. Am J Physiol Heart Circ Physiol. 297(1): H208–H222.

Saito M, Ikenaga Y, Matsukawa M, Watanabe Y, Asada T, Lagrée P-Y. 2011. One-dimensional model for propagation of a pressure wave in a model of the human arterial network: comparison of theoretical and experimental results. J Biomech Eng. 133:121005.

Segers P, Stergiopulos N, Verdonck P, Verhoeven R. 1997. Assessment of distributed arterial network models. Med Biol Eng Comput. 35(6):729–736.

Sherwin SJ, Formaggia L, Peiro J, Franke V. 2003. Computational modelling of 1D blood flow with variable mechanical properties and its application to the simulation of wave propagation in the human arterial system. Int J Numer Methods Fluids. 43(6–7):673–700.

Shu CW. 2001. Different formulations of the discontinuous Galerkin method for the viscous terms. In: Advances in scientific computing. p. 144–155.

Shu CW, Osher S. 1988. Efficient implementation of essentially non-oscillatory shock-capturing schemes. J Comput Phys. 77(2):439–471.

Steele BN, Wan J, Ku JP, Hughes TJ, Taylor CA. 2003. In vivo validation of a one-dimensional finite-element method for predicting blood flow in cardiovascular bypass grafts. IEEE Trans Biomed Eng. 50(6):649–656.

Stergiopulos N, Young DF, Rogge TR. 1992. Computer simulation of arterial flow with applications to arterial and aortic stenoses. J Biomech. 25(12):1477–1488.

Stettler JC, Niederer P, Anliker M. 1981. Theoretical analysis of arterial hemodynamics including the influence of bifurcations. Ann Biomed Eng. 9(2):145–164.

Torii R, Oshima M, Kobayashi T, Takagi K, Tezduyar TE. 2006. Fluid–structure interaction modeling of aneurysmal conditions with high and normal blood pressures. Comput Mech. 38(4–5):482–490.

Vignon IE, Taylor CA. 2004. Outflow boundary conditions for one-dimensional finite element modeling of blood flow and pressure waves in arteries. Wave Motion. 39(4):361–374.

Wan J, Steele B, Spicer SA, Strohband S, Feijo GR, Hughes TJR, Taylor CA. 2002. A one-dimensional finite element method for simulation-based medical planning for cardiovascular disease. Comput Methods Appl Mech Eng. 5(3):195–206.

Wang JJ, Parker KH. 2004. Wave propagation in a model of the arterial circulation. J Biomech. 37(4):457–470.

Wang X, Delestre O, Fullana J-M, Saito M, Ikenaga Y, Matsukawa M, Lagrée P-Y. 2012. Comparing different numerical methods for solving arterial 1D flows in networks. Comput Methods Appl Mech Eng. 15(Suppl 1):61–62.

Wibmer M. 2004. One-dimensional simulation of arterial blood flow with applications [PhD thesis]. Vienna, Austria: Vienna University of Technology.

Yomosa S. 1987. Solitary waves in large blood vessels. J Phys Soc Jpn. 56:506–520.

Zagzoule M, Marc-Vergnes J-P. 1986. A global mathematical model of the cerebral circulation in man. J Biomech. 19(12):1015–1022.